10018100-1-F

WAVE-COHERENCE MEASUREMENTS USING SYNTHETIC APERTURE RADAR

FINAL REPORT

November 2000

D.T. Walker
D.R. Lyzenga

Prepared for:

Office of Naval Research
800 North Quincy Street
Arlington, VA 22217-5660

Contract Number: N00014-98-C-0012

VERIDIAN
ERIM International

P.O. Box 134008 Ann Arbor, MI 48113-4008 734-994-1200
www.erim-int.com

TECHNICAL REPORT STANDARD TITLE PAGE

1. Report No. 10018100-1-F	2. Government Accession No.	3. Recipient's Catalog No.
4. Title and Subtitle WAVE-COHERENCE MEASUREMENTS USING SYNTHETIC APERTURE RADAR		5. Report Date NOVEMBER 2000
		6. Performing Organizational Code
7. Author(s) DAVID T. WALKER, DAVID R. LYZENGA		8. Performing Organizational Report No. 10008100-1-F
9. Performing Organization Name and Address Veridian-ERIM International Incorporated PO Box 134008 Ann Arbor, Michigan 48113-4008		10. Work Unit No.
		11. Contract or Grant No. N00014-98-C-0012
12. Sponsoring Agency Name and Address Office of Naval Research Ballston Tower One 800 North Quincy Street Arlington, Virginia 22217-5660		13. Type of Report and Period Covered Final-September 1998 to September 2000
		14. Sponsoring Agency Code
15. Supplementary Notes		

16. Abstract

A critical issue in the design of large floating structures, such as those being considered in the Mobile Offshore Base (MOB) effort currently being pursued by the US Navy, is the nature of the ocean-wave field, viewed on scales of 2 km or more. Of prime concern is the ability to assess the spatial 'coherence' of the wave field, or the probability of occurrence of long, unbroken wave crests for various environmental conditions. This report describes an effort to use satellite-based synthetic-aperture radar images to determine the crest-length statistics for ocean waves. The first portion of the study examined the feasibility of using SAR image data to determine the crest length distribution, which was shown the be directly related to the directional spread of the spectrum. A fully nonlinear SAR model was used in a simulation study to assess the impact of imaging effects on the resulting measures. For the cases examined, the errors in estimated directional spread were generally less than 20-30% and were conservative when the SAR look direction was within 20° of the propagation direction. The errors were shown to increase with increasing significant wave height, increasing directional spread, and increasing angle between the wave propagation direction and the SAR look direction. The second portion of the study developed a methodology to estimate the wave spectrum directly from the SAR-image spectrum via a variational inversion procedure. The methodology was successful, and the results from ERS SAR data indicate that errors in spectral parameters such as the mean wave length and directional spread are strongly dependent on the signal to noise ratio, as measured by the peak image spectral density. Errors become large when the peak spectral density falls below about 10 m2 for ERS SAR data. Above this level, estimates of wave length and directional spread are accurate to within about 10-20%.

17a. Key Words synthetic aperture radar, wave spectrum, wave coherence	18. Distribution Statement Approved for public release; distribution unlimited.		
19. Security Classif. (of this report) Unclassified	20. Security Classif. (of this page) Unclassified	21. No. of Pages iv + 59	22. Price

ABSTRACT

A critical issue in the design of large floating structures, such as those being considered in the Mobile Offshore Base (MOB) effort currently being pursued by the US Navy, is the nature of the ocean-wave field, viewed on scales of 2 km or more. Of prime concern is the ability to assess the spatial 'coherence' of the wave field, or the probability of occurrence of long, unbroken wave crests for various environmental conditions. This report describes an effort to use satellite-based synthetic-aperture radar images to determine the crest-length statistics for ocean waves. The first portion of the study examined the feasibility of using SAR image data to determine the crest length distribution, which was shown the be directly related to the directional spread of the spectrum. A fully nonlinear SAR model was used in a simulation study to assess the impact of imaging effects on the resulting measures. For the cases examined, the errors in estimated directional spread were generally less than 20–30% and were conservative when the SAR look direction was within 20° of the propagation direction. The errors were shown to increase with increasing significant wave height, increasing directional spread, and increasing angle between the wave propagation direction and the SAR look direction. The second portion of the study developed a methodology to estimate the wave spectrum directly from the SAR-image spectrum via a variational inversion procedure. The methodology was successful, and the results from ERS SAR data indicate that errors in spectral parameters such as the mean wave length and directional spread are strongly dependent on the signal to noise ratio, as measured by the peak image spectral density. Errors become large when the peak spectral density falls below about 10 m^2 for ERS SAR data. Above this level, estimates of wave length and directional spread are accurate to within about 10–20%.

Table of Contents

List of Figures

INTRODUCTION

This study examines the feasibility of using remote sensing data to characterize wave coherence, in order to provide needed environmental data for the design of mobile off-shore bases (MOB). The remote sensing methodology of interest is satellite-based synthetic-aperture radar (SAR) This report summarizes work in two main areas. First, the use of SAR imagery directly to determine quantities related to wave coherence is examined, and the impact of SAR-imaging effects on the resulting estimated quantities is assessed. The second part of the study examines a method for circumventing the limitations imposed by the SAR-imaging effects. A variational inversion method is developed and used to estimated the wave height spectrum with only the SAR-image spectrum as input. Estimates of spectral characteristics from the wave spectrum thus determined are shown to be more accurate than corresponding estimates obtained directly from the SAR-image spectra.

The first portion of the study examined the feasibility of using SAR image data to determine quantities related to wave coherence. The quantity of primary interest was the crest length distribution, which was shown the be directly related to the directional spread of the spectrum. It was of interest to determine whether the apparent crest length distribution, or directional spreading, seen in a SAR image of ocean waves reflected those of the actual ocean waves, and if so, under what conditions can wave coherence be determined directly from the SAR imagery. Simulated SAR-image spectra based on unimodal (swell-like) wave-height spectra were calculated using a fully nonlinear SAR-image spectrum model. A range of wave conditions and sensor geometries were examined and the imaging effects were identified. For the cases examined, the errors were generally within 20–30% and were conservative (in that the wave crest lengths were over-estimated) when the SAR look direction was within 20° of the

propagation direction. It was also shown that the apparent wave propagation direction in the SAR imagery, was a good estimate of the actual wave propagation direction. The errors were shown to increase with increasing significant wave height, increasing directional spread, and increasing angle between the wave propagation direction and the SAR look direction.

The second portion of the study developed a methodology to estimate the actual wave spectrum directly from the SAR-image spectrum via a variational inversion procedure. The methodology was successful in the sense that it is able to determine a wave height spectrum that produces a SAR-image spectrum which agrees with the observed image spectrum; however, it is also true that in many cases this is not a unique solution, and in several cases it obviously misses waves that are outside the azimuth passband of the SAR. The results indicate that errors in spectral parameters such as the mean wave length and direction are strongly dependent on the signal to noise ratio, as measured by the peak image spectral density. Mean errors are small, but the random error becomes large when the peak spectral density falls below about 10 m^2 for ERS SAR data (this level is dependent on the spatial resolution, assuming the dominant noise source is coherent speckle). Above this level, estimates of wave length and directional spread are accurate to within about 10–20%.

ESTIMATING WAVE COHERENCE FROM SAR IMAGERY

In this portion of the study, the primary measure of wave coherence used is the crest-length distribution. We first examine the relationship between crest length statistics and wave spectral measures, and then address the question of how well these spectral measures can be estimated from remote sensing data. The remote sensing technologies considered here are satellite-based synthetic-aperture radar (SAR) for observing the spatial pattern of the wave field, and satellite-based microwave altimetry for measuring the significant wave height and wind speed. These satellite-based microwave sensors can 'see through' clouds and operate independent of the weather.

SAR images possess the spatial resolution and area coverage needed to obtain coherence data relevant to these large-scale MOBs, and coincident altimeter observations can provide information on sea state. The main concern in using SAR image data for coherence measures is that some the wave information is lost, or modified, in the SAR imaging process. These SAR imaging effects are most pronounced for short waves; nevertheless, their importance for the large-scale waves of interest in MOB design needs to be considered. The SAR-imaging effects, and how they are manifested in the SAR image spectrum, can be largely determined *a priori*, given knowledge of the significant wave height (obtained from coincident altimeter data), and the sensor viewing geometry. The objective of this study is to determine the range of viewing geometries and significant wave heights which will yield reliable estimates of crest-length statistics, and to quantify the errors introduced by SAR-imaging effects.

1 Background

1.1 SAR Imaging of Ocean Waves

A number of radar techniques have been developed to measure ocean wave directional spectra [1]. For the conditions under which most SAR systems operate, the principal radar scattering mechanism from the ocean surface is Bragg scattering, which is controlled by the amplitude or spectral density of surface waves having wavelengths comparable to that of the electromagnetic radiation (typically a few centimeters). These Bragg waves are modulated by their interaction with the orbital velocities associated with longer surface waves, and this produces a variation in backscatter that more or less follows the profile of the long waves. The radar backscatter also varies locally because of the 'tilting' of the surface by the long waves, since the backscatter is a strong function of local incidence angle. This tilting effect produces a backscatter modulation that is approximately proportional to the long-wave slope. The spatial or temporal spectrum of the backscatter is therefore expected to be approximately proportional to the wave spectrum. This relationship is observed experimentally, although the constant of proportionality (the modulation transfer function) tends to be somewhat larger than is predicted using existing hydrodynamic and electromagnetic scattering models [2].

The motion of the ocean surface influences SAR images because the Doppler shift of the returned signal is used to resolve the surface in the cross-range or azimuthal direction. Random surface motions therefore limit the effective azimuthal resolution of the images. When the image is Fourier transformed in order to estimate the wave spectrum, this results in a loss of information at high wavenumbers, thus limiting the spectral bandwidth of the SAR image spectrum in the azimuthal direction. This loss of information at high azimuthal wavenumbers is called the 'azimuth fall-off' effect. The orbital motions associated with long ocean waves also

cause a modulation of the image intensity through the 'velocity-bunching' effect which under some conditions can increase the contrast of the wave images. For large-amplitude waves or large R/V ratios (where R is the range distance and V is the SAR platform velocity), however, this relationship becomes nonlinear, resulting in the generation of harmonics and other image artifacts. This nonlinearity and the 'azimuth fall-off' due to random surface motions constitute the chief difficulties in relating the SAR image spectrum to the wave spectrum [3].

1.2 Anticipated Impact of SAR Imaging Effects on Coherence Measures

The SAR image spectrum differs from the ocean wave spectrum in two significant ways. First, the azimuth fall-off effect removes the high wavenumber waves in the along-track direction. The width of the pass-band depends primarily on the significant wave height and can be estimated, given that information. Secondly, there may be distortions of the spectral shape within the pass-band, due to the wavenumber dependence of the modulation transfer function. For example, the interaction of the tilt, hydrodynamic and velocity-bunching modulations can result in a 'null' in the spectrum along a line passing through the origin of the spectrum, slightly oblique to the look direction [4]. These effects are also largely predictable, given the sensor viewing geometry and the environmental conditions.

The impact of these SAR imaging effects on the resulting coherence estimates may vary, depending upon the direction of the dominant waves relative to the SAR look direction, as well as the wave length and wave height. Knowing the nature and magnitude of these effects allows us to determine when they are significantly influencing the coherence measures. It should be noted that since long-crested seas are potentially more destructive (by inducing large torsional moments in the MOB) than short-crested seas, an overestimate of the coherence length would be considered a conservative error.

1.3 Altimeter Observations of Sea State

Satellite radar altimeters operate by transmitting short pulses of microwave radiation vertically downward toward the ocean surface and measuring the time history of the returned pulses. The time of arrival of the returned pulse is used, along with highly accurate measurements of the satellite position, to obtain the mean surface elevation, from which geostrophic currents and subsurface topography can be inferred. Secondly, the amount of energy in the returned pulse is a measure of the small-scale surface roughness, from which the wind speed can be estimated. Finally, from the rise time or distortion of the returned pulse shape, the large-scale surface elevation variance or significant wave height can be calculated. Measurements of the wave height obtained from altimetry data agree well with *in situ* measurements, but are limited to average values over the surface area intercepted by the incident pulse, which is typically a few tens of kilometers.

1.4 Availability of SAR and Altimeter Data

SAR and altimetry data are available from archival sources as well as from ongoing collections with currently operational sensors. Recent and current SAR sensors include the European Remote Sensing satellites ERS-1 and ERS-2, and the Canadian RADARSAT. The ERS satellites include altimetry as well as SAR data but there is an offset of about 250 km between the side-looking SAR images and the nadir-looking altimeter, which limits the usefulness of the simultaneously collected SAR and altimetry data. Other sources of altimetry data include the Geosat and Topex/Poseidon satellites. Thus, there is a rich source of information that can potentially be tapped for this application. Selection of contemporaneous, co-located data sets is a non-trivial task, however.

2 Crest Length Statistics

In order to investigate the relationship between crest length statistics and wave spectral measures, surface realizations were constructed for various wave spectra. The realizations were constructed by choosing complex Fourier amplitudes such that the real and imaginary parts are each normally distributed with mean values of zero and variances equal to half the wave height spectral density at a given wavenumber. These amplitudes were then Fourier transformed to obtain surface elevation maps with sample spacings of 12.5 meters, to correspond to the pixel spacings of ERS SAR images. Figure 1a shows a narrow-banded sea surface generated from a Gaussian-shaped spectrum with a directional spread of 0.1 radians, a center frequency of 0.08 Hz and a width of 0.008 Hz.

The resulting elevation maps were processed by passing them through an algorithm that classifies each contiguous set of pixels with elevations greater than one standard deviation as a wave crest. Figure 1b shows the wave crests identified by this procedure, using the elevation map in Figure 1a. The length of each crest was measured and the lengths were binned to form histograms. The histograms were then summed and normalized by the scene area, so as to form an estimate of the number of crests per unit area with lengths greater than L, where L varies from zero to a maximum length that is typically a third or so of the scene length. An example of the resulting crest length distribution, for the surface elevation map in Figure 1a, is shown in Figure 1c. The shape of this distribution function, which is typical of all the cases considered, can be approximated by the equation

$$N(L) = N_o e^{-L/L_o}, \tag{1}$$

where L is the crest length and N is the number of crests per km^2 with lengths greater than L. The parameters describing this distribution are the scale length (L_o) and the total number of wave

crests per km^2 (N_o). It can be seen that L_o is equal to the mean crest length if this equation adequately fits the data. We estimated this parameter by computing a linear least-squares fit to the logarithm of the observed distribution function.

By measuring the crest length distributions for a range of wave spectra, a relationship was found between the mean or characteristic crest length, L_o, the dominant wavelength, λ, and the angular spread of the wave spectrum, $\Delta\phi$. This relationship, as shown in Figure 2, can be approximated by the equation

$$\frac{L_o}{\lambda} \approx \frac{0.35}{\Delta\phi} \tag{2}$$

where $\Delta\phi$ is defined as the full width of the spectrum at half the maximum value.

3 SAR Imaging Effects

To investigate the effects of SAR imaging on wave coherence measures, a series of forward predictions of the SAR image spectrum were carried out using the Hasselmann formulation [5,6]. Simulations were made over a range of significant wave heights (2–10 m), dominant wave frequencies (0.06–0.09 Hz), and SAR look directions relative to the wave propagation direction. An assumed Gaussian expected-value wave-height spectrum was used as input to the Hasselmann model; the output from the model was then the expected value of the SAR-image spectrum. The directional spread of this expected-value SAR-image spectrum is the calculated, and compared to that of the original wave spectrum. Since the directional spread is calculated from the expected-value spectrum, and not a realization from the spectrum, there is no scatter in the results. The SAR parameters for the simulations were those typical of satellite SAR sensors (specifically the European Space Agency's ERS platform).

Figure 3 shows the apparent directional spread of the SAR spectrum, divided by the directional spread of the actual wave spectrum, as a function of the SAR look direction relative to the dominant wave direction for two significant wave heights. These results are for a narrow wave spectrum ($\Delta\phi$=0.105 rad). The significant wave heights shown are H_s = 2 m, a moderate wave height, and H_s = 10 m, typical of severe weather conditions. The figure shows that for H_s = 2 m, the error in directional spread (and hence in the crest-length distribution) is less than 10%. For H_s = 10 m, the errors are as large as 30% near a relative look angle of 20°. The apparent narrowing of the wave spectrum is due to the narrow azimuth pass band associated with the SAR imaging process, and the resulting modification of the shape of the image spectrum. It should be noted that these errors are conservative in the sense that the directional spread is underestimated, and so the crest lengths are overestimated.

Figure 4 shows similar plots for the same spectral width but a shorter wavelength, λ = 200 m, and wave heights H_s = 2 m, 5 m and 10 m. For H_s = 2 m, the error in apparent directional spread increases with SAR look direction and levels off at about 30% low for angles greater than 20°. For H_s = 5 m the errors are similar for look directions near the wave propagation direction but then the apparent spread increases monotonically for look directions beyond 20°. The apparent widening of the spectrum occurs when the peak of the wave spectrum moves outside of the SAR pass band. For H_s = 10 m the errors become large more rapidly, with the directional spread being overestimated for look directions greater than 20°.

Figure 5 shows the corresponding results for a broader wave spectrum ($\Delta\phi$=0.245 rad) with a 500 m dominant wavelength. The significant wave heights shown are again H_s = 2 m, 5 m and 10 m. For all wave heights, the error increases with look direction and again becomes constant at an apparent directional spread which is about 30–40% low near a relative look angle of 20°.

Again, the apparent narrowing of the wave spectrum is due to the narrow azimuth pass band associated with the SAR imaging process, and the consequent distortion of the wave spectrum. The errors for this case are also conservative.

Similar plots for a shorter wavelength, $\lambda = 200$ m, again with the broad spectrum are shown in Figure 6. The results are similar to those shown in figure 4 for the narrow directional spectrum, except that for $H_s = 10$ m, the directional spread is underestimated for small look directions by more than 40%.

4 Estimating Wave Direction

From the foregoing, it is clear that the reliability of estimating the directional spread of the wave spectrum from the SAR spectrum depends on the significant wave height, and the look direction of the SAR sensor relative to the wave direction. The significant wave height can be determined from contemporaneous satellite altimeter data. The only available information on the wave direction is in the SAR image data itself. Since the SAR imaging effects modify the shape of the wave spectrum, it is reasonable to expect that the apparent wave direction can differ from the actual wave direction. The accuracy of estimating the wave propagation direction from the SAR image data will now be addressed.

The apparent wave direction can be determined from the location of the peak in the SAR spectrum. Figure 7 shows the apparent wave direction plotted versus SAR look direction for the narrow spectrum conditions of figures 3 and 4, with a wavelength of 500 m. From the figure, it is clear that the wave direction can be estimated within a few percent from the SAR spectrum under all conditions. Similar results for a wavelength of 200 m are shown in figure 8. The errors for this case are slightly larger, but the conclusion is again that the wave direction can be estimated accurately from the SAR spectrum.

5 Application to Actual Sar Data

5.1 Labrador Sea

The methodology described above was applied to two ERS SAR images. Figure 9a shows an ERS image collected on 23 March 1997 over the Labrador Sea, at approximately 57° N and 52° W. The significant wave height, as measured on the nearest Topex/Poseidon altimeter pass was approximately 6.4 m. In order to reduce the effects of low-frequency trends as well as high-frequency speckle noise in the images, a Fourier threshold filter was applied to the data before running the crest recognition algorithm. This filter operates by computing the image spectrum, locating the peak in the spectrum, and zeroing out all Fourier components having a power less than one tenth of the peak value. The resulting crest map is shown in Figure 9b.

The crest length distribution obtained from this data set is shown in Figure 9c. The shape of this distribution is fit quite closely by equation (1) with L_o=360 m and N_o=5 wave crests per km^2. This distribution implies that there are approximately 0.02 wave crests per km^2 with crest lengths greater than 2 km. The dominant wavelength observed in the image spectrum for this case was about 400 m, which translates into a peak period of 16 sec. The directional spreading was relatively broad (about 0.3 rad) for this case, because the region of high winds generating these waves was large and quite near the observation region. For the observed 0.3 rad directional spread, $L_o/\lambda \approx 1.1$ would be expected from (2); this is slightly larger than the observed value of $L_o/\lambda \approx 0.9$, but indicates that the crest length distribution is closely related to the directional spread of the spectrum. This small discrepancy may be due to the Fourier threshold filtering.

5.2 Oregon Coast

The second SAR image, shown in Figure 10a, was collected on 24 December 1995 off the coast of Oregon, at approximately 44.5° N and 124.5° W. The significant wave height measured by a nearby NOAA/NDBC buoy was approximately 3.3 m, and the peak period was 16.7 sec. The Fourier threshold filter was applied to this image and the crest recognition algorithm was run on the filtered data, resulting in the crest map shown in Figure 10b.

The crest length distribution for this data, as shown in Figure 10c, is characterized by the parameters L_o=1220 m and N_o=1 per km^2. This distribution implies that the number of wave crests with crest lengths greater than 2 km is approximately 0.2 per km^2, which is an order of magnitude larger than that for the Labrador Sea image. The reason for the larger number of long crests is of course the narrowness of the spectrum, which is related to the distance from the storm generating these waves. The spectral width for this case was estimated to be about 0.1 radians, which is about one third of the width for the Labrador Sea data. Here, for the observed 0.1 rad directional spread, $L_o/\lambda \approx 3.5$ would be expected from (2); again this is comparable, but slightly larger than the observed value of $L_o/\lambda \approx 2.8$.

6 Conclusions of the First Portion of the Study

The conclusions of this study are as follows:

1) For 500 m waves, spectral widths derived from SAR are within 20–30%. The errors are conservative (spectral width underestimated, or crest lengths overestimated).

2) For 200 m waves with $H_s < 5$ m, spectral widths derived from SAR are within 20% for wave directions within ~10° of the SAR look direction, and within 40% for wave directions up to 45°. Errors tend to be conservative.

3) For 200 m waves $H_s > 5$ m, spectral widths derived from SAR are within 50% for wave directions within ~20° of the SAR look direction.

4) In all cases, error in the estimated spectral width increases with the actual spectral width.

5) The apparent wave direction can be determined accurately from the SAR-image spectrum for all wave heights.

INVERSION OF SAR SPECTRA TO OBTAIN WAVE SPECTRA

A number of studies have been conducted over the past 25 years on the relationship between SAR images of the ocean surface and the wave height spectrum. A milestone in this research was the publication of a closed-form expression for the expected value of the SAR image spectrum in terms of the autocorrelation functions of the radial velocity and the radar cross section and the cross-correlation of these quantities [5],[6]. These correlation functions can be related to the wave height spectrum, using linear wave theory and a radar modulation transfer function, thus allowing a forward prediction of the image spectrum from the wave height spectrum.

Various efforts have also been made to invert this relationship in order to estimate the wave height spectrum from measurements of the SAR image spectrum. Some efforts [9],[10] have used a reduced form of this relationship, referred to as the quasi-linear model, in order to simplify the inversion procedure. Other efforts [5],[11]-[14] have used the full nonlinear theory combined with some sort of *a priori* or external information, such as a prescribed form for the spectrum or a first-guess spectrum based on wave model predictions, in order to alleviate problems associated with the loss of information in the image spectrum due to nonlinearities in the imaging process. These procedures result in estimates of the wave height spectrum which are a mixture of the information provided by the SAR image and the *a priori* information. To our knowledge, a solution of the "pure" inversion problem, *i.e.* a determination of the wave height spectrum that reproduces the observed image spectrum without any *a priori* information, has not previously been reported in the literature.

In this paper, we describe a relatively straightforward procedure for inverting the Hasselmann expression so as to obtain a wave height spectrum that is consistent with a given

SAR image spectrum, with no additional constraints or *a priori* information except for the overall wave propagation direction (*i.e.* a selection of one of the two peaks in the folded SAR image spectrum). The inversion procedure is first evaluated using simulated data, by calculating the image spectra for an assumed set of wave height spectra, applying the inversion algorithm to these image spectra, and comparing the results with the assumed wave height spectra. The algorithm is then applied to a set of ERS SAR images collected under a range of wave conditions. In this way, the question of the adequacy of the inversion procedure is addressed separately from that of the forward model.

1 Forward Prediction

The expression for the predicted image spectrum derived by Hasselmann and Hasselmann [5] and Krogstad [6] can be written in a slightly modified form as

$$\hat{S}_i(k_x,k_y) = \tfrac{1}{(2\pi)^2}\iint G(x,y,k_x)e^{-i(k_x x+k_y y)}dx\,dy$$

where

$$G(x,y,k_x) = \left\{\rho_{rr}(x,y) + f(x,y,k_x)f(-x,-y,-k_x)\right\}e^{-k_x^2 C(x,y)}$$

$$f(x,y,k_x) = 1 + ik_x[\rho_{rv}(x,y) - \rho_{rv}(0,0)]$$

$$C(x,y) = \rho_{vv}(0,0) - \rho_{vv}(x,y)$$

$$\rho_{rr}(x,y) = \mathrm{Re}\iint \left|T_r(k_x,k_y)\right|^2 S(k_x,k_y)e^{i(k_x x+k_y y)}dk_x dk_y$$

$$\rho_{rv}(x,y) = \mathrm{Re}\iint T_r(k_x,k_y)T_v^*(k_x,k_y)S(k_x,k_y)e^{i(k_x x+k_y y)}dk_x dk_y$$

$$\rho_{vv}(x,y) = \mathrm{Re}\iint \left|T_v(k_x,k_y)\right|^2 S(k_x,k_y)e^{i(k_x x+k_y y)}dk_x dk_y$$

$$T_r(k_x,k_y) = k\,m(k_x,k_y) \text{ and } T_v(k_x,k_y) = \frac{R}{V\sigma}\left(gk_y\sin\theta - i\sigma^2\cos\theta\right).$$

Here $S(k_x, k_y)$ is the wave height spectrum, x and y are the azimuth and range coordinates and k_x

and k_y are the corresponding wavenumbers, σ is the wave frequency, g is the gravitational acceleration, R is the range distance, V is the SAR platform velocity, and θ is the incidence angle.

The function $m(k_x, k_y)$ is the radar modulation transfer function (mtf), which describes the variations in the radar backscatter due to surface tilt and hydrodynamic effects. In our implementation, we have used a modification of the expressions given by Plant and Zurk [10] for the radar mtf. The modifications are to (1) divide the mtf by tanh(kd), where d is the water depth, thus effectively referencing the backscatter modulations to the surface height or slope instead of the orbital velocity, (2) use a $\cos^2\phi$ angular dependence for the hydrodynamic mtf, as suggested by wave-current interaction theory, instead of the $|\cos\phi|$ dependence used by Plant and Zurk, (3) neglect the term in their expression for the tilt mtf that is intended to account for wind wave directionality effects, and (4) reverse the sign of the tilt mtf so as to be consistent with the sign convention expressed by the equation $m = m_h + i\, m_t$. With these modifications, the tilt modulation transfer function is given by

$$m_t = \left\{5\cot\theta + 4\tan\theta - \frac{4\sin\theta}{\cos\theta + n}\right\}\cos(\phi - \phi_r)$$

for horizontal polarization, and

$$m_t = \left\{5\cot\theta + 4\tan\theta - \frac{4n\sin\theta}{n\cos\theta + 1} - \frac{4\sin\theta\cos\theta}{1+\sin^2\theta}\right\}\cos(\phi - \phi_r)$$

for vertical polarization where θ is the incidence angle, ϕ is the long wave propagation direction, ϕ_r is the radar look direction, and $n \approx 9$ for sea water.

The hydrodynamic mtf is given by the Plant and Zurk empirical formula, which can be written with our modifications as

$$m_h = \frac{m_o}{\tanh Kd}\sqrt{\frac{g}{U\Omega}}\cos^2(\phi - \phi_r)$$

where U is the wind speed, Ω is the wave frequency, $m_o = 7.5$ for vertical polarization and $m_o = 12.5$ for horizontal polarization. As pointed out by Plant and Zurk, this polarization dependence indicates that this is not a true hydrodynamic mtf and should more properly be termed a "residual" mtf.

2 Inversion Procedure

The inversion procedure investigated here involves adjusting the wave height spectrum $S(\bar{k})$ so as to make the predicted and observed image spectra as nearly equal as possible, *i.e.* to minimize the cost function

$$J = \int [\hat{S}_i(\bar{k}) - S_i(\bar{k})]^2 d\bar{k}$$

where $\hat{S}_i(\bar{k})$ is the predicted image spectrum and $S_i(\bar{k})$ is the observed image spectrum. The change in the cost function due to a change in the wave spectrum is given by

$$\delta J = 2\int [\hat{S}_i(\bar{k}) - S_i(\bar{k})]\delta\hat{S}_i(\bar{k})\, d\bar{k}$$

where $\delta\hat{S}_i$ represents the change in the predicted image spectrum due to a change δS in the wave spectrum. This change can be written as

$$\delta\hat{S}_i(\bar{k}) = \int R(\bar{k},\bar{k}')\delta S(\bar{k}')d\bar{k}'$$

where $R(\bar{k},\bar{k}')$ is the incremental or differential transfer function discussed in Appendix A. Substituting this into the above equation for δJ, we have

$$\delta J = 2\iint [\hat{S}_i(\bar{k}) - S_i(\bar{k})]R(\bar{k},\bar{k}')\delta S(\bar{k}')d\bar{k}d\bar{k}' = \int P(\bar{k}')\delta S(\bar{k}')d\bar{k}'$$

where

$$P(\bar{k}') = 2\int [\hat{S}_i(\bar{k}) - S_i(\bar{k})]R(\bar{k},\bar{k}')d\bar{k}.$$

Note that $P(\bar{k}')$ can be considered as the gradient of the cost function with respect to the variable $S(\bar{k}')$. Thus, we can reduce the cost function by changing the wave spectrum by the amount $\delta S(\bar{k}') = -\varepsilon P(\bar{k}')$ where $\varepsilon > 0$. Our procedure is then to start with an initial estimate of the spectrum (usually zero), calculate $\hat{S}_i(\bar{k})$ and $P(\bar{k})$, change the spectrum by $\delta S(\bar{k}) = -\varepsilon P(\bar{k})$ and repeat until J is minimized. An important question, however, is how to choose ε in order to reach this minimum most efficiently.

One approach for choosing the step size is to approximate the transfer function as discussed in Appendix B, which reduces the cost function gradient to

$$P(\bar{k}) = 2\Delta S_i(\bar{k})\, R_\ell(\bar{k})$$

where

$$\Delta S_i(\bar{k}) = \hat{S}_i(\bar{k}) - S_i(\bar{k}) \quad \text{and} \quad R_\ell(\bar{k}) = \left\{ |T_r(\bar{k})|^2 + k_x^2 |T_v(\bar{k})|^2 \right\} e^{-k_x^2 \rho_w(0)}.$$

Choosing $\delta S(\bar{k}) = -\varepsilon P(\bar{k})$, the corresponding change in the predicted image spectrum is then

$$\delta\hat{S}_i(\bar{k}) = -\varepsilon \int R(\bar{k},\bar{k}')P(\bar{k}')d\bar{k}' \approx -\varepsilon[R_\ell^2(\bar{k}) + R_\ell^2(-\bar{k})]\Delta\hat{S}_i(\bar{k}).$$

To choose the step size we note that for small ε, the cost function can be written as

$$J(\varepsilon) = \int [\hat{S}_i(\bar{k}) + \delta\hat{S}_i(\bar{k}) - S_i(\bar{k})]^2 d\bar{k} = J_0 - J_1\varepsilon + J_2\varepsilon^2$$

where

$$J_0 = \int [\hat{S}_i(\bar{k}) - S_i(\bar{k})]^2 d\bar{k},$$

$$J_1 = 2\int [R_\ell^2(\bar{k}) + R_\ell^2(-\bar{k})][\hat{S}_i(\bar{k}) - S_i(\bar{k})]^2 d\bar{k},$$

$$J_2 = \int [R_\ell^2(\bar{k}) + R_\ell^2(-\bar{k})]^2[\hat{S}_i(\bar{k}) - S_i(\bar{k})]^2 d\bar{k}.$$

This function has a minimum at

$$\varepsilon = \frac{J_1}{2J_2} = \frac{\int [R_\ell^2(\vec{k}) + R_\ell^2(-\vec{k})][\hat{S}_i(\vec{k}) - S_i(\vec{k})]^2 d\vec{k}}{\int [R_\ell^2(\vec{k}) + R_\ell^2(-\vec{k})]^2 [\hat{S}_i(\vec{k}) - S_i(\vec{k})]^2 d\vec{k}}.$$

Although the actual cost function may not be minimized at this location because of nonlinear effects, results obtained to date indicate this to be a reasonable choice for ε.

Inclusion of nonlinear effects results in a second term in the cost function gradient which essentially involves a convolution of the prediction error $\Delta S_i(\vec{k})$ with the current estimate of the wave spectrum. Two forms of this term are derived in Appendix B, under the assumptions that the wave spectrum is either very broad or is concentrated at very low azimuth wavenumbers. In principle, using a refined expression for the cost function gradient would be expected to speed up convergence, at the expense of some additional computations for each iteration. In practice, however, no appreciable speedup in convergence has been observed with either of these forms and so the linearized expression has been used to compute the cost function gradient for all the cases presented in this paper (note that the full nonlinear transformation is used for the forward predictions to compute the cost function at each iteration). Note also that the factor $e^{-k_x^2 \rho_{vv}(0)}$ in the cost function gradient receives contributions from both the 'resolved' and 'unresolved' portions of the wave spectrum. The contribution from the 'unresolved' portion, which we define as the region $|k_x| > \pi/\Delta x$ and $|k_y| > \pi/\Delta y$ where Δx and Δy are the sample spacings in the SAR image, can be computed using $S(\vec{k}) = (\alpha/4\pi)k^{-4}$ with $\alpha = 0.0081$, which is consistent with the high-frequency region of the Pierson-Moskowitz spectrum. This yields

$$\rho_{vv}(0) = g\left(\frac{R}{V}\right)^2 \int_{-\pi}^{\pi}\int_{k_c}^{\infty} k\left[\sin^2\phi \sin^2\theta + \cos^2\theta\right] S(k)\, k\, dk\, d\phi = \frac{\alpha g}{4\pi}\left(\frac{R}{V}\right)^2 \left(1 + \cos^2\theta\right)\Delta x.$$

Our experience using actual ERS data has led to a modification of this procedure, however, as

discussed below. The contribution from the resolved part of the spectrum is obtained by integrating the current estimate of the wave spectrum at each iteration.

3 Results using Simulated SAR Data

Simulated SAR image spectra were calculated for set of six cases in order to illustrate the response of the inversion algorithm to nonlinearities in the imaging process. The peak wavelength was set at 100 meters, and peak wave directions of 20° and 40° from the range direction were chosen, with significant wave heights of 0.5 m, 1.0 m, and 1.5 m. These cases clearly do not span the entire range of possible conditions but were chosen to be representative of the actual ERS cases examined in the following section. Wave height spectra were calculated using a two-dimensional Gaussian function with a fractional width of 0.2 in the wavenumber direction and an angular width of 15°. Figures 11 and 12 show the input wave height spectra (left column), the simulated image spectra (center column), and the wave height spectra estimated from these image spectra (right column), after 50 iterations of the inversion algorithm.

The effects of nonlinearities can be seen in the image spectra as a decrease in the image spectral density, relative to the wave height spectral density, as the wave height increases (downward on each figure) and as a flattening or rotation of the image spectra relative to the wave height spectra. Typical ERS SAR parameters were used for the image spectrum calculations, with an R/V ratio of about 120 sec, a 23° incidence angle, vertical polarization, and a pixel spacing of 12.5 m. A wind speed of 5 m/s (for calculation of the radar mtf) and a sub-resolution scale rms velocity of 0.3 m/s was used in all cases.

For the 20° case, the estimated wave spectra are quite close to the input wave spectra in all cases, even in the presence of moderate nonlinearities. For the 40° case, however, there is a clear loss of energy in the estimated wave spectrum as the wave height increases (the significant wave

height is underestimated by about 30 percent in the worst case). This does not necessarily mean that the inversion procedure failed in these cases however. Even in the worst case, the cost function after 50 iterations was reduced by a factor of 40 below its original value, which indicates that the SAR image spectrum calculated from the estimated wave height spectrum agrees very closely with the input image spectrum. This is illustrated in Figure 13, which shows the simulated image spectrum used as input into the inversion algorithm on the left, and the image spectrum calculated from the estimated wave height spectrum on the right. The two spectra are almost indistinguishable, indicating that the procedure was successful in determining a wave height spectrum that is consistent with the input image spectrum. The fact that this spectrum is not the same as the original wave spectrum used as input into the simulation is a vivid illustration of the non-unique (many-to-one) nature of the SAR imaging process.

Presumably there is an infinite set of wave height spectra, of which those shown in the lower right and lower left panels of Figure 12 are only two examples, that are consistent with the same image spectrum (shown in the lower center panel). In such cases, some additional information is required to select the most appropriate solution among the possible solutions. An optimal procedure for doing this has yet to be developed. The practical importance of this problem, as compared to other effects (such as speckle noise, geophysical noise, and thermal noise) and uncertainties in important parameters (such as the radar mtf and the sub-resolution scale velocity variance) is not yet clear, and motivates the analysis of actual SAR data as discussed in the following section.

4 Results using ERS SAR Data

An evaluation of the inversion procedure was conducted using a set of 14 ERS-1 and ERS-2 images collected near the US Army Corps of Engineers Field Research Facility (FRF) in Duck,

North Carolina. The directional wave spectrum is measured at the FRF by means of an array of nine pressure sensors located about 900 meters offshore, at a depth of 8 meters [13]. Directional information is computed from these gauges using an iterative maximum likelihood estimator [14], [15]. For comparison with the ERS spectra, which were extracted in deeper water, the FRF spectra were transformed using the equation

$$S_1(\omega,\phi_1) = \frac{k_1}{k_0}\frac{c_{g1}}{c_{g0}} S_1(\omega,\phi_0)$$

where $c_{gi} = \partial\omega / \partial k_i$, $\omega = gk_0 \tanh k_0 d_0 = gk_1 \tanh k_1 d_1$, and $k_0 \sin\phi_0 = k_1 \sin\phi_1$, ϕ being the wave propagation direction relative to the shore normal [18]. The directional frequency spectra were converted into the corresponding wavenumber spectra

$$S_1(k,\phi) = \frac{c_g}{k} S_\omega(\omega,\phi)$$

which were then rotated and resampled onto a rectangular wavenumber grid corresponding to the ERS spectra.

The dates of the ERS overpasses are shown in Table 1, along with the water depths in the ERS subsets used for analysis, the significant wave height, the mean wave length and direction, and the mean wind speed and direction. All of these were descending passes, with overpass times close to 15:44 GMT, and so the FRF wave spectra and wind speeds recorded at 10:00 EST on the day of each overpass were used. The wave spectra were transformed into the locations at which the ERS spectra were measured, as described above. The mean wave lengths and directions were obtained from these transformed wavenumber spectra using an algorithm that first locates the spectral peak and finds the set of contiguous wavenumber samples with spectral densities larger than half of this peak value. The centroid of this set of samples is computed from its spectral moments, and converted into a mean wavenumber k_m and direction ϕ_m. The

Table 1. ERS overpass dates, with corresponding wave and wind parameters obtained from FRF measurements.

Date	d (m)	H_s (m)	λ_m (m)	ϕ_m (deg T)	U_w (m/s)	ϕ_w (deg T)
28 May 1996	21.7	1.27	112	-117	2.4	-1
29 May 1996	19.7	0.87	94	-115	1.4	48
03 July 1996	17.9	0.69	104	-79	4.1	-94
07 Aug 1996	18.0	0.56	84	-56	3.5	74
11 Sep 1996	18.2	0.34	174	-92	3.2	-5
16 Oct 1996	23.0	0.48	125	-91	3.9	-142
25 Dec 1996	17.6	1.37 (0.53)	60 (102)	-152 (-66)	8.0	-2
05 Mar 1997	17.9	1.12	112	-117	3.3	76
09 Apr 1997	17.9	1.36 (0.40)	53 (83)	-157 (-101)	9.7	6
14 May 1997	27.8	0.56	102	-57	3.4	-134
18 June 1997	17.1	0.54	111	-106	5.4	-133
27 Aug 1997	21.0	0.74	89	-109	5.7	37
05 Nov 1997	20.2	0.99 (0.51)	54 (123)	-153 (-100)	5.1	35
10 Dec 1997	19.8	0.42	80	-56	5.8	93

mean wave length is $\lambda_m = 2\pi/k_m$, and the direction ϕ_m represents the direction toward which the waves are propagating (the oceanographic convention). The wind speeds and directions shown in Table 1 were measured using an anemometer located at the end of the FRF pier at an elevation of 19 m. The wind directions represent those from which the wind is blowing (the meteorological convention).

For three of these data sets (25 Dec 1996, 09 Apr 1997, and 05 Nov 1997) the spectrum was bimodal, with a wind wave peak that was clearly outside the azimuth passband of the ERS SAR. For these three data sets, a second version of the wave spectrum was also computed by removing the wave energy corresponding to azimuth wavenumbers larger than 0.0628 rad/m. The spectral parameters for these modified spectra are shown in parentheses in Table 1.

The ERS images were examined to locate the 512x512 pixel regions nearest to the FRF pier that were uncontaminated by extraneous image features such as those induced by wind speed variations, slicks, fronts, internal waves, etc. The latitude and longitude of the corner points of

each of these regions were determined by interpolation from the nominal image corner locations, and the mean water depth within each region was determined using the Duck94 digital bathymetry data set. These depths, shown in the second column of Table 1, were used to control the FRF wave spectrum transformation described above.

The image spectrum was computed by dividing each region into sixteen 128x128 pixel subsets. The mean image intensity within each subset was converted into the 'modulation' function $f(x,y) = I(x,y)/\bar{I} - 1$ where $\bar{I}$ is the mean image intensity for each subset. The 2-D Fourier transform was computed, the squared magnitude of the Fourier transform was taken, and the resulting sixteen spectra were averaged together. The spectra were normalized such that the sum of the spectral densities, multiplied by $\Delta k_x \Delta k_y$, is equal to the variance of the 'modulation' image, where $\Delta k_x = \Delta k_y = 2\pi / L$ is the wavenumber sample spacing, $L = N\Delta x = N\Delta x$, N =128, and $\Delta x = \Delta x = 12.5$ m is the ERS image sample spacing. Next, the same procedure was applied to a uniform region taken from inside Albemarle Sound. A smoothed version of this spectrum was first obtained by Fourier transforming it (to obtain the covariance function), zeroing out all values of the covariance less than 1/10 of the maximum value, and inverse transforming. This smoothed spectrum was then used to correct the wave image spectra for both speckle background and stationary impulse response function (resolution) effects, by subtracting it from and dividing it into each the wave image spectra. Finally, the corrected spectra were smoothed by convolving them with a 2-D Gaussian filter having a width (standard deviation) of one sample. For reference, grayscale plots of the resulting image spectra are shown in Figure 17.

These image spectra were used in the wave spectrum inversion procedure described in section 3, using zero as the initial estimate for the wave spectrum. The measured wind speeds, as well as the water depths, were used in the procedure to calculate the radar modulation transfer

function. During preliminary experimentation with the procedure, it was found that the results are not highly dependent on the magnitude of this transfer function, since the image modulations are frequently dominated by velocity bunching effects. However, the results were found to be quite sensitive to the value assumed for the unresolved velocity variance, represented by the $''$ term discussed in the previous section. Optimal results were obtained in many cases by using values smaller than the nominal value that is calculated by assuming a saturated spectrum for the unresolved waves. To deal with this problem, a procedure was implemented whose objective is to estimate this quantity from the image spectrum itself [19], [20]. Briefly, the image autocorrelation function is first computed by Fourier transforming the image spectrum. The central part of the autocorrelation function is fit, in the azimuth direction, by a Gaussian function of the form $C(x) = \exp(-\pi x / \lambda_c)^2$ and the velocity variance is computed from

$$\rho_{ww}(0) = \left(\frac{R}{V}\right)^2 \sigma_v^2 = \left(\lambda_c / \pi\right)^2 .$$

This procedure resulted in estimates of σ_v ranging from 0.22 to 0.38 m/s. Using these values in the inversion algorithm resulted in better overall performance than any constant value that was tried.

The inversion algorithm was allowed to continue for 50 iterations for each data set (the average cpu time was about 1.8 seconds for each run, or about 0.036 seconds per iteration, on a Sun workstation). A composite plot of the cost function versus the number of iterations is shown in Figure 14. We have not fully investigated the question of when to stop the iteration, but several possible convergence criteria could be envisioned, including the absolute value of the cost function, the cost function value relative to its initial value, or the rate of change of the cost function. It would appear from Figure 14 that a relative threshold is more appropriate than an

absolute one, although a rate of change might also be used. For these cases, the cost function after 50 iterations averages about 1/14 of its initial value. In some cases the cost function has levelled off after 10-20 iterations, while in other cases the cost function is still decreasing at 50 iterations even though its value is quite small relative to the initial value.

To compare these results with the FRF spectra, the latter were rotated into the ERS coordinate system, assuming the along-track direction to be 191.9 °T for all the ERS passes. Gray scale maps of the estimated wave spectra and the transformed FRF spectra for each case are shown in Figure 18.

The wave parameters shown in Table 1 were also extracted from the estimated wave height spectra, and are compared with the corresponding parameters from the FRF spectra in Figures 15 and 16. Figure 15 shows the differences between the mean wavenumber and direction, and the ratios of the spectral widths in wavenumber and direction obtained from the estimated wave height spectra and from the corresponding FRF spectra, plotted versus the peak spectral density in the ERS image spectra. The peak spectral density is a measure of the strength of the signal relative to the speckle noise background, and seems to be the single variable that is most strongly related to the errors or differences in the spectral measures shown. It is apparent from these plots that the magnitude of these differences become smaller as the signal level increases. Thus, the primary source of error in these spectral measures would appear to be random noise, probably that associated with coherent speckle effects. The mean error in wavenumber for these data sets is –0.008 rad/m, and the rms error is 0.016 rad/m. The mean error in wave direction is –3.2 °, and the rms error is 24.6 ° for the entire data set.

Figure 16 shows the significant wave heights (defined as $H_s = 4\sigma_h$, where σ_h^2 is the integral of the wave height spectrum over all wavenumbers) obtained from the estimated spectra versus

those obtained from the FRF spectra. For the three cases containing wind wave spectral peaks outside the ERS passband, the FRF wave heights were computed using only the energy within the passband, as shown in Table 1. The wave height within the passband is estimated with about the same accuracy for these cases (indicated in Figure 16 with the $\oplus$ symbol) as in the other cases. The mean error in H_s for all of the data sets is 0.01 m, and the rms error is 0.14 m.

5 Conclusions from the Second Portion of the Study

The inversion procedure described in this paper is mathematically successful in almost all the cases encountered, in the sense that it is able to determine a wave height spectrum that agrees with the observed image spectrum when it is used as an input into the forward prediction model. However, it is also true that in many cases this is not a unique solution, and in several cases it obviously misses waves that are outside the azimuth passband of the SAR. We have started with zero as an initial estimate, and have accounted for the effects of unresolved waves by means of a procedure that estimates these effects directly from the data. Given this procedure, the solution appears to be unique. However, it would be possible to start with a different initial estimate (for example an isotropic, saturated spectrum) and it is quite clear that the final results would be quite different. We have not investigated this question in detail, but suggest that it might be possible to place error bounds on the estimated spectrum by comparing the results for two radically different initial estimates.

Our results indicate that errors in spectral parameters such as the mean wave length and direction are strongly dependent on the signal to noise ratio, as measured by the peak image spectral density. Mean errors are small, but the random error becomes large when the peak spectral density falls below about 10 m^2 for ERS SAR data (this level is dependent on the spatial resolution, assuming the dominant noise source is coherent speckle). The significant wave

height estimated from the image spectrum appears to be somewhat less sensitive to noise, since the error in H_s is not observed to be highly correlated with the signal level. The rms error in H_s for this data set was 0.14 m, excluding wind wave spectral peaks that were clearly outside the passband of the SAR.

ACKNOWLEDGEMENT

The ERS SAR data used in this study was obtained under the European Space Agency's Announcement of Opportunity (AO3) program. FRF spectra were obtained from the U.S. Army Corps of Engineers (http://frf.usace.army.mil), and the Duck94 digital bathymetry data set was provided by Dr. Robert Jensen of the U.S. Army Waterways Experiment Station. Thanks also to Mr. Marc Renouf and Ms. Nicole Miller for processing the ERS image spectra, and to Dr. Merrick Haller for extracting the water depths at the subset locations, and computing the transformed FRF spectra at these locations.

APPENDIX A. INCREMENTAL SAR TRANSFER FUNCTION

The inversion procedure discussed in this paper requires an expression for the change in the predicted SAR image spectrum $\hat{S}_i(\vec{k})$ due to a small change in the wave height spectrum from $S(\vec{k})$ to $S(\vec{k}) + \delta S(\vec{k})$. To derive such an expression, we first consider the effect of a change in the wave spectrum of the form

$$\delta S(\vec{k}) = \frac{\varepsilon}{2\pi\sigma^2} e^{-\frac{1}{2}|\vec{k}-\vec{k}''|^2/\sigma^2}$$

which implies a change ε in the height variance, with most of the change occurring near the wavenumber $\vec{k}''$. For mathematical convenience, we then allow σ to approach zero, which yields

$$\delta S(\vec{k}) = \varepsilon\delta(\vec{k} - \vec{k}'') = \varepsilon\delta(k_x - k_x'')\delta(k_y - k_y'').$$

This change in the wave spectrum produces changes in the correlation functions ρ_{rr}, ρ_{vv}, and ρ_{rv} as given by

$$\delta\rho_{rr}(\vec{x}) = \varepsilon \mid T_r(\vec{k}'') \mid^2 \cos(\vec{k}'' \cdot \vec{x}), \quad \delta\rho_{vv}(\vec{x}) = \varepsilon \mid T_v(\vec{k}'') \mid^2 \cos(\vec{k}'' \cdot \vec{x}), \quad \text{and}$$

$$\delta\rho_{rv}(\vec{x}) = \varepsilon \mathrm{Re}\left\{ T_r^*(\vec{k}'')T_v(\vec{k}'')\right\} \cos(\vec{k}'' \cdot \vec{x}) + \varepsilon \mathrm{Im}\left\{ T_r^*(\vec{k}'')T_v(\vec{k}'')\right\} \sin(\vec{k}'' \cdot \vec{x}).$$

The corresponding change in the predicted image spectrum can be written as

$$\delta\hat{S}_i(\vec{k}) = \frac{1}{(2\pi)^2}\iint \delta G(\vec{x}, k_x) e^{-i\vec{k}\cdot\vec{x}} d\vec{x}$$

where

$$\delta G(\vec{x}, k_x) = \left\{\delta\rho_{rr}(\vec{x}) + \delta F(\vec{x}, k_x) + \delta F(-\vec{x}, -k_x)\right\} e^{-k_x^2 C(\vec{x})} - k_x^2 G(\vec{x}, k_x)\delta C(\vec{x}),$$

$$\delta F(\vec{x}, k_x) = ik_x f(\vec{x}, k_x)\left[\delta\rho_{rv}(0) - \delta\rho_{rv}(-\vec{x})\right], \quad \text{and} \quad \delta C(\vec{x}) = \delta\rho_{vv}(0) - \delta\rho_{vv}(\vec{x}).$$

To evaluate this expression, we use the approximation

$$e^{-k_x^2 C(\vec{x})} \approx e^{-k_x^2 \rho_{vv}(0)} + \left[1 - e^{-k_x^2 \rho_{vv}(0)}\right] e^{-\frac{1}{2}(\sigma_x^2 x^2 + \sigma_y^2 y^2)}$$

where

$$\sigma_x^2\left[1 - e^{-k_x^2 \rho_{vv}(0)}\right] = k_x^2 \frac{\partial^2 C}{\partial x^2}(0) = k_x^2 \iint k_x'^2 \mid T_v(k_x', k_y') \mid^2 S(k_x', k_y')\, dk_x' dk_y'$$

and

$$\sigma_y^2\left[1 - e^{-k_x^2 \rho_{vv}(0)}\right] = k_x^2 \frac{\partial^2 C}{\partial y^2}(0) = k_x^2 \iint k_y'^2 \mid T_v(k_x', k_y') \mid^2 S(k_x', k_y')\, dk_x' dk_y'.$$

To simplify further, we note that the cross-correlation function $\rho_{rv}(\vec{x})$ is typically an order of magnitude or so smaller than the auto-correlation functions $\rho_{rr}(\vec{x})$ and $\rho_{vv}(\vec{x})$, and consequently we neglect second-order terms involving ρ_{rv}. The change in the image spectrum can then be written as

$$\delta S_i(\vec{k}) = \frac{1}{(2\pi)^2} e^{-k_x^2 \rho_{vv}(0)} \iint g(\vec{x}, k_x) e^{-i\vec{k}\cdot\vec{x}} d\vec{x} + \frac{1}{(2\pi)^2}\left[1 - e^{-k_x^2 \rho_{vv}(0)}\right] \iint g(\vec{x}, k_x) e^{-i\vec{k}\cdot\vec{x} - \frac{1}{2}(\sigma_x^2 x^2 + \sigma_y^2 y^2)} d\vec{x}$$

where

$$g(\vec{x}, k_x) = \delta\rho_{rr}(\vec{x}) + ik_x[\delta\rho_{rv}(\vec{x}) - \delta\rho_{rv}(-\vec{x})] + k_x^2[1 + \rho_{rr}(\vec{x})][\delta\rho_{vv}(\vec{x}) - \delta\rho_{vv}(0)].$$

The first integral can be evaluated as

$$\iint g(\vec{x}, k_x) e^{-i\vec{k}\cdot\vec{x}} d\vec{x} = 2\pi^2 \varepsilon[R_0(\vec{k}, \vec{k}'')\delta(\vec{k} - \vec{k}'') + R_0(-\vec{k}, \vec{k}'')\delta(\vec{k} + \vec{k}'')]$$

$$+2\pi^2 k_x^2 \varepsilon \mid T_v(\vec{k}'') \mid^2 [S_{rr}(\vec{k} - \vec{k}'') + S_{rr}(\vec{k} + \vec{k}'') - 2S_{rr}(\vec{k})]$$

where

$$R_0(\vec{k}, \vec{k}'') = \left| T_r(\vec{k}'') + ik_x T_v(\vec{k}'') \right|^2$$

and

$$S_{rr}(\vec{k}) = \frac{1}{(2\pi)^2} \iint \rho_{rr}(\vec{x}) e^{-i\vec{k}\cdot\vec{x}} d\vec{x} = \frac{1}{2}\left\{ \mid T_r(\vec{k}) \mid^2 S(\vec{k}) + \mid T_r(-\vec{k}) \mid^2 S(-\vec{k}) \right\}$$

This implies that a change in the wave spectrum at a single wavenumber ($\vec{k}''$) produces changes in the predicted image spectrum at a range of wavenumbers, which is of course a consequence of the nonlinearity of the imaging process. The terms involving $R_0(\vec{k},\vec{k}'')$ describe the portion of the wave energy that is mapped into the image spectrum at the same wavenumber (the linear response), while the remaining terms describe the diffusion of the wave energy into other regions of the image spectrum due to nonlinear effects. Note that if the wave spectrum has a sharp peak at the wavenumber $\vec{k}_o$, an increase in the wave spectrum at the wavenumber $\vec{k}''$causes a transfer of energy in the image spectrum from the region near $\pm\vec{k}_o$ to the wavenumbers $\vec{k} = \pm\vec{k}_o \pm \vec{k}''$ due to nonlinear effects, as well as a direct increase at $\vec{k} = \pm\vec{k}''$due to the linear response.

A second class of nonlinear effects is represented by the second integral in the above expression for $\delta\hat{S}_i(\vec{k})$. Neglecting the term involving $\rho_{rr}(\vec{x})$, this integral can also be evaluated analytically using the relationship

$$\int_{-\infty}^{\infty} e^{-ikx-\kappa^2 x^2}\,dx = \frac{\sqrt{\pi}}{\kappa}\, e^{-\frac{k^2}{4\kappa^2}}$$

to yield

$$\iint g(\vec{x},k_x)e^{-i\vec{k}\cdot\vec{x}-\frac{1}{2}(\sigma_x^2x^2+\sigma_y^2y^2)}d\vec{x} = 2\pi^2\varepsilon[R_0(\vec{k},\vec{k}'')\bar{\delta}(\vec{k},\vec{k}'')+R_0(-\vec{k},\vec{k}'')\bar{\delta}(-\vec{k},\vec{k}'')]$$

where

$$\bar{\delta}(\vec{k},\vec{k}'') = \frac{1}{2\pi\sigma_x\sigma_y}\exp\left\{-\frac{1}{2}\left[(k_x-k_x'')^2/\sigma_x^2+(k_y-k_y'')^2/\sigma_y^2\right]\right\}.$$

Note that this set of terms has the effect of merely smearing or blurring the linear response function rather than redistributing the energy nonlocally. The term involving $\rho_{rr}(\vec{x})$ produces a blurred version of the nonlocal/nonlinear response function described above, as can be shown by

using the representation

$$\rho_{rr}(\vec{x}) = \iint S_{rr}(\vec{k}')e^{i\vec{k}'\cdot\vec{x}}d\vec{k}' \ .$$

The term in question can then be written as

$$\iint k_x^2 \rho_{rr}(\vec{x})[\delta\rho_{vv}(\vec{x}) - \delta\rho_{vv}(0)]e^{-i\vec{k}\cdot\vec{x} - \frac{1}{2}(\sigma_x^2 x^2 + \sigma_y^2 y^2)}d\vec{x}$$

$$= \varepsilon k_x^2 \mid T_v(\vec{k}'') \mid^2 \iint\iint S_{rr}(\vec{k}')[\cos(\vec{k}''\cdot\vec{x}) - 1]e^{-i(\vec{k}-\vec{k}')\cdot\vec{x} - \frac{1}{2}(\sigma_x^2 x^2 + \sigma_y^2 y^2)}d\vec{x}\,d\vec{k}'$$

$$= 2\pi^2 \varepsilon k_x^2 \mid T_v(\vec{k}'') \mid^2 \iint S_{rr}(\vec{k}')[\bar{\delta}(\vec{k},\vec{k}'+\vec{k}'') + \bar{\delta}(\vec{k},\vec{k}'-\vec{k}'') - 2\bar{\delta}(\vec{k},\vec{k}')]d\vec{k}'$$

$$= 2\pi^2 \varepsilon k_x^2 \mid T_v(\vec{k}'') \mid^2 \iint [S_{rr}(\vec{k}'-\vec{k}'') + S_{rr}(\vec{k}'+\vec{k}'') - 2S_{rr}(\vec{k}')]\bar{\delta}(\vec{k},\vec{k}')d\vec{k}'$$

$$= 2\pi^2 \varepsilon k_x^2 \mid T_v(\vec{k}'') \mid^2 [\bar{S}_{rr}(\vec{k}-\vec{k}'') + \bar{S}_{rr}(\vec{k}+\vec{k}'') - 2\bar{S}_{rr}(\vec{k})].$$

The effect of an arbitrary (small) change in the wave spectrum $\delta S(\vec{k}')$ can now be obtained by summing or integrating the responses due to a change at a single wavenumber, *i.e.*

$$\delta\hat{S}_i(\vec{k}) = \int R(\vec{k},\vec{k}')\delta S(\vec{k}')d\vec{k}'$$

where $R(\vec{k},\vec{k}')$ is the response to a delta-function change in the wave spectrum, as discussed above. This can be seen by substituting $\delta S(\vec{k}') = \varepsilon\delta(\vec{k}'-\vec{k}'')$ into this equation. Equating the resulting value of $\delta\hat{S}_i(\vec{k}) = \varepsilon R(\vec{k},\vec{k}'')$ with that derived earlier in this appendix, we obtain

$$R(\vec{k},\vec{k}') = \tfrac{1}{2}[R_1(\vec{k},\vec{k}') + R_1(-\vec{k},\vec{k}')] + \tfrac{1}{2}k_x^2 \mid T_v(\vec{k}') \mid^2 [S_1(\vec{k},\vec{k}') + S_1(\vec{k},-\vec{k}') - 2S_1(\vec{k},0)]$$

where

$$R_1(\vec{k},\vec{k}') = \left| T_r(\vec{k}') + ik_x T_v(\vec{k}') \right|^2 \left\{ e^{-k_x^2\rho_w(0)}\delta(\vec{k}-\vec{k}') + \left[1 - e^{-k_x^2\rho_w(0)}\right]\bar{\delta}(\vec{k},\vec{k}') \right\}$$

and

$$S_1(\vec{k},\vec{k}') = \left\{ e^{-k_x^2\rho_w(0)}\, S_{rr}(\vec{k}-\vec{k}') + \left[1 - e^{-k_x^2\rho_w(0)}\right]\bar{S}_{rr}(\vec{k}-\vec{k}') \right\} .$$

APPENDIX B. COMPUTATION OF THE COST FUNCTION GRADIENT

Using the incremental transfer function derived in Appendix A, the cost function gradient can be written as

$$P(\vec{k}') = 2\int [\hat{S}_i(\vec{k}) - S_i(\vec{k})]R(\vec{k},\vec{k}')d\vec{k}.$$

Evaluation of this gradient requires an accurate computation of the predicted image spectrum at each iteration, but some approximation of the transfer function $R(\vec{k},\vec{k}')$appears to be acceptable. More accurate computation of this transfer function may speed up the convergence, but the time gained by faster convergence must be balanced against the number of computations required at each iteration. One approximation is to retain only the first term in the transfer function, *i.e.*

$$R(\vec{k},\vec{k}') \approx \tfrac{1}{2}\left|T_r(\vec{k}') + ik_x T_v(\vec{k}')\right|^2 [\delta(\vec{k}-\vec{k}') + \delta(\vec{k}+\vec{k}')]e^{-k_x^2\rho_w(0)},$$

which is sometimes referred to as the quasi-linear SAR transfer function. The cost function gradient for this case can be written (substituting $\vec{k}$ for $\vec{k}'$) as

$$P(\vec{k}) = 2\,\Delta S_i(\vec{k})\left\{\,|T_r(\vec{k})|^2 + k_x^2\,|T_v(\vec{k})|^2\right\} e^{-k_x^2\rho_w(0)}$$

where

$$\Delta S_i(\vec{k}) = \hat{S}_i(\vec{k}) - S_i(\vec{k}).$$

Analytic expressions that include nonlinear effects can also be developed for the limiting cases $\sigma_x,\sigma_y \to 0$ and $\sigma_x,\sigma_y \to \infty$. In the first case $\bar{\delta}(\vec{k},\vec{k}') \to \delta(\vec{k}-\vec{k}')$ and $\bar{S}_{rr}(\vec{k},\vec{k}') \to S_{rr}(\vec{k},\vec{k}')$, and the transfer function reduces to

$$R(\vec{k},\vec{k}') \approx \tfrac{1}{2}\left|T_r(\vec{k}') + ik_x T_v(\vec{k}')\right|^2 [\delta(\vec{k}-\vec{k}') + \delta(\vec{k}+\vec{k}')]$$

$$+\tfrac{1}{2}k_x^2\,|\,T_v(\vec{k}')\,|^2\,[S_{rr}(\vec{k}-\vec{k}') + S_{rr}(\vec{k}+\vec{k}') - 2S_{rr}(\vec{k})].$$

The cost function gradient for this case can be written as

$$P(\vec{k}) = 2\,\Delta S_i(\vec{k})\left\{\,|T_r(\vec{k})|^2 + k_x^2\,|T_v(\vec{k})|^2\right\} + \left\{\,F(\vec{k}) + F(-\vec{k}) - 2F(0)\right\}\,|\,T_v(\vec{k})\,|^2$$

where

$$F(\vec{k}) = \frac{1}{(2\pi)^2}\iint \Delta\rho_i(\vec{x})\rho_{rr}(\vec{x})e^{-i\vec{k}\cdot\vec{x}}d\vec{x} \quad \text{and} \quad \Delta\rho_i(\vec{x}) = \iint k_x^2\,\Delta S_i(\vec{k})e^{i\vec{k}\cdot\vec{x}}d\vec{k}\,.$$

In the second case ($\sigma_x, \sigma_y \to \infty$), $\overline{\delta}(\vec{k},\vec{k}') \to 0$ and $\overline{S}_{rr}(\vec{k},\vec{k}') \to 0$. This results in the same expression for the cost function gradient but with $\Delta S_i(\vec{k})$ multiplied by the factor $e^{-k_x^2\rho_{vv}(0)}$.

REFERENCES

1. Jackson, F.C. and D.R. Lyzenga, "Microwave Techniques for Measuring Directional Wave Spectra," Chapter 14 in *Surface Waves and Fluxes*, ed. by G.L. Geernaert and W.J. Plant, Kluwer Pub. Co., Amsterdam, 1990.

2. Plant, W.J. and L.M. Zurk, "Dominant wave directions and significant wave heights from synthetic-aperture radar imagery of the ocean," *J. Geophys. Res.* **102**, 3473–3482, 1997.

3. Lyzenga, D.R. "The Physical Basis for Estimating Wave Energy Spectra from SAR Imagery," *Johns Hopkins APL Technical Digest* **8**, 65-69, 1987.

4. Bruning, C., W. Alpers, L.F. Zambresky, and D.G. Tilley, "Validation of synthetic-aperture radar ocean wave imaging theory by the Shuttle Imaging Radar–B experiment over the North Sea," *J. Geophys. Res.* **93**, 15 403–15 425, 1988.

5. Hasselmann, K. and S. Hasselmann, "On the nonlinear mapping of an ocean wave spectrum into a synthetic aperture radar image spectrum and its inversion," *J. Geophys. Res.* **96**, 10 713–10 729, 1991.

6. Krogstad, H.E., "A simple derivation of Hasselmann's nonlinear ocean-to-synthetic aperture radar transform," *J. Geophys. Res.* **97**, 2421–2425, 1992.

7. F.M. Monaldo and D.R. Lyzenga, "On the estimation of wave slope- and height-variance spectra from SAR imagery," *IEEE Trans. Geosci. Remote Sensing*, vol. GE-24, pp. 543-551, July 1986.

8. W.J. Plant and L.M. Zurk, "Dominant wave directions and significant wave heights from synthetic aperture radar imagery of the ocean," *J. Geophys. Res.*, vol. 102, no. C2, pp. 3473-3482, 1997.

9. G. Engen, H. Johnsen, H.E. Krogstad, and F. Barstow, "Directional wave spectra by inversion of ERS-1 synthetic aperture radar ocean imagery," *IEEE Trans. Geosci. Remote Sensing*, vol. 32, pp. 340-352, March 1994.

10. H. Krogstad, O. Samset, and P. Vachon, "Generalizations of the nonlinear ocean-SAR transform and a simplified SAR inversion algorithm," *Atmos. Ocean*, vol. 32 , pp. 61-82, 1994.

11. S. Hasselmann, C. Brüning, K. Hasselmann, and P. Heimbach, "An improved algorithm for the retrieval of ocean wave spectra from synthetic aperture radar image spectra," *J. Geophys. Res.*, vol 101, no. C7, pp. 16615-16629, 1996.

12. C. Mastenbroek and C.F. de Valk, "A semiparametric algorithm to retrieve ocean wave spectra from synthetic aperture radar," *J. Geophys. Res.*, vol. 105, no. C2, pp. 3497-3516, 2000.

13. C. Long and J. Oltman-Shay, "Directional characteristics of waves in shallow water," *Technical Report CERC-91-1*, US Army Engineer Waterways Experiment Station, Vicksburg, MS, 1991.

14. S. Pawka, "Island shadows in directional wave spectra," *J. Geophys. Res.*, vol. 88, no. C4, pp. 2579-2591, 1983.

15. C. Long and J. Atmadja, "Index and bulk parameters for frequency-direction spectra measured at CERC Field Research Facility, September 1990 to August 1991," *Miscellaneous Paper CERC-94-5*, US Army Engineer Waterways Experiment Station, Vicksburg, MS, 1994.

16. B. LeMéhauté and J.D. Wang, "Wave spectrum changes on sloped beach," *J. Waterway, Port, Coastal and Ocean Div., ASCE,* vol. 103, pp. 33-47, 1982.

17. V. Kerbaol, B. Chapron, and P.W. Vachon, "Analysis of ERS-1/2 synthetic aperture radar wave mode imagettes," *J. Geophys. Res.*, vol. 103 , no. C4, pp. 7833-7846, 1998.

18. E. Korsbakken, J.A. Johannessen, and O.M. Johannessen, "Coastal wind field retrievals from ERS synthetic aperture radar images," *J. Geophys. Res.*, vol. 103 , no. C4, pp. 7857-7874, 1998.

FIGURES

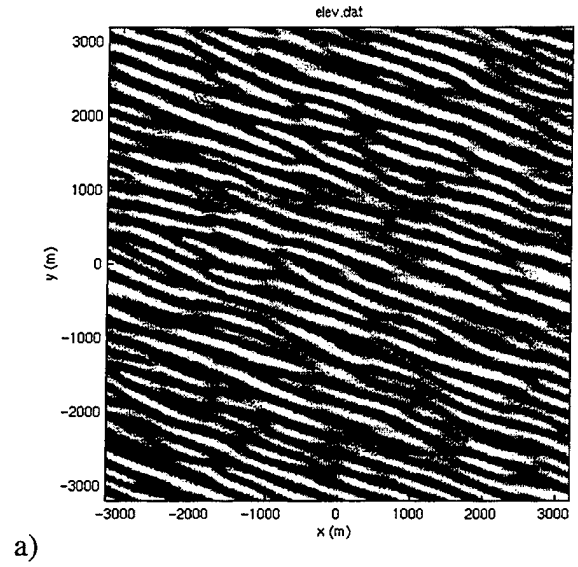

a)

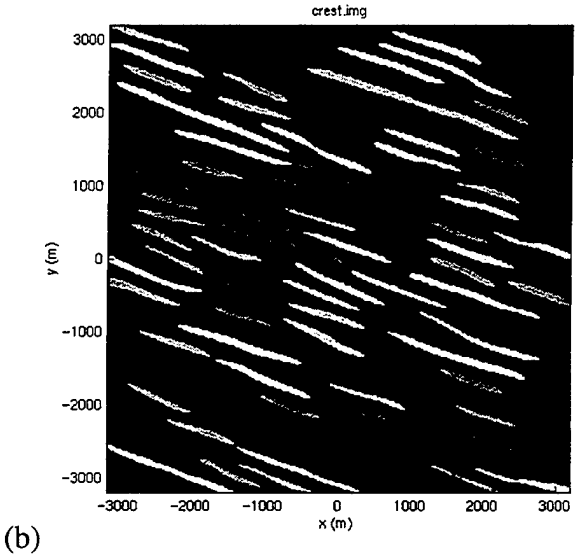

(b)

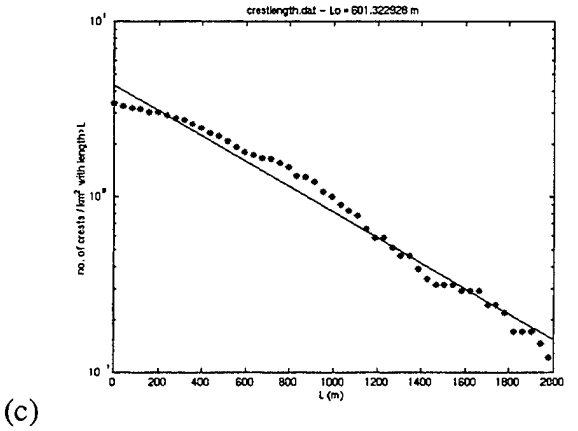

(c)

Figure 1 Simulated sea surface and identified crests; a) simulated sea surface, b) wave crests identified sea surface, and c) crest length distribution.

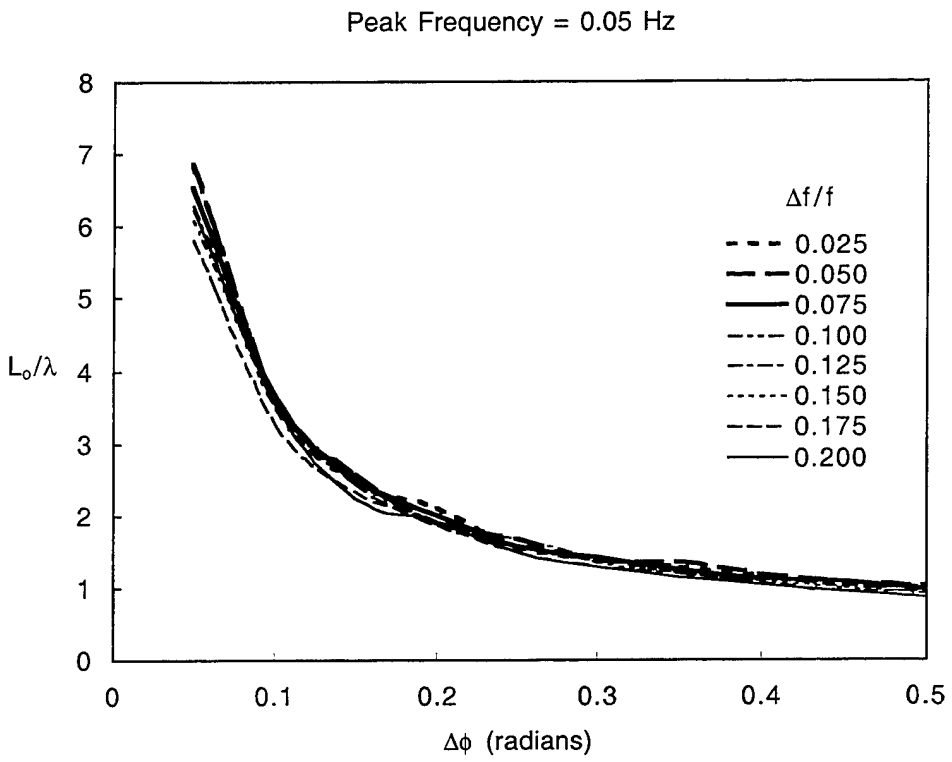

Figure 2 Crest length distributions as a function of directional spread $\Delta\phi$ for various spectral widths $\Delta f/f$ and a peak frequency of 0.05 Hz.

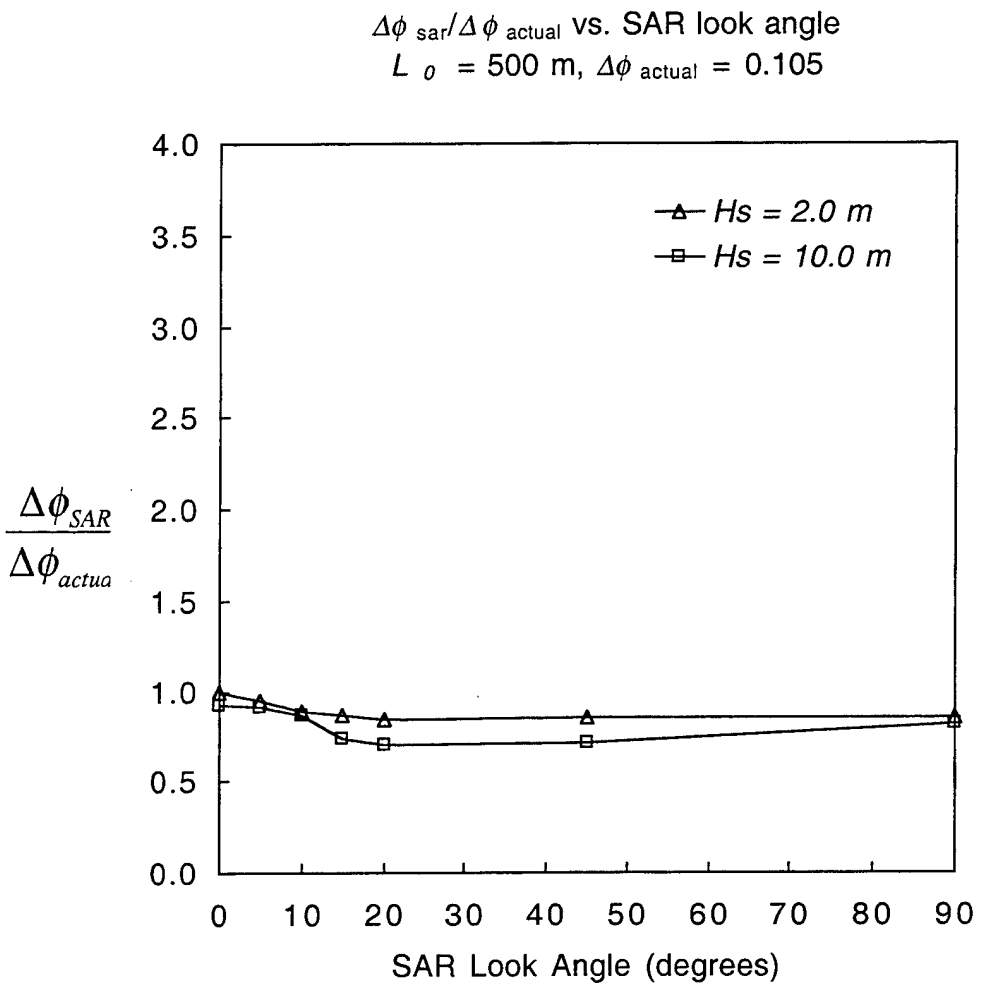

Figure 3 Apparent directional spread $\Delta\phi_{SAR}$ from simulated SAR image, normalized by actual directional spread $\Delta\phi_{Actual} = 0.105$ for various SAR look directions relative to the dominant wave direction, with H_s = 2.0 m and 10.0 m, and λ = 500 m.

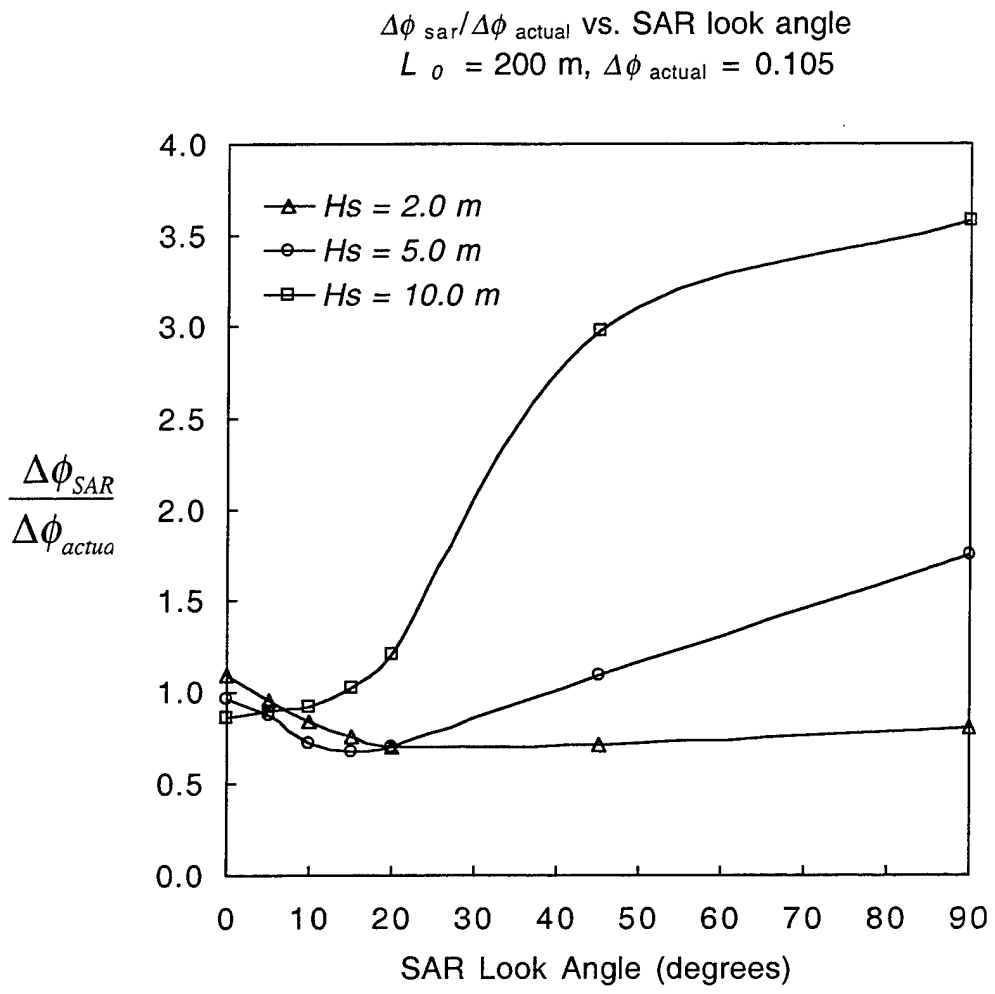

Figure 4 Apparent directional spread $\Delta\phi_{SAR}$ from simulated SAR image, normalized by actual directional spread $\Delta\phi_{Actual} = 0.105$ for various SAR look directions relative to the dominant wave direction, with H_s = 2.0 m, 5 m and 10.0 m, and λ = 200 m.

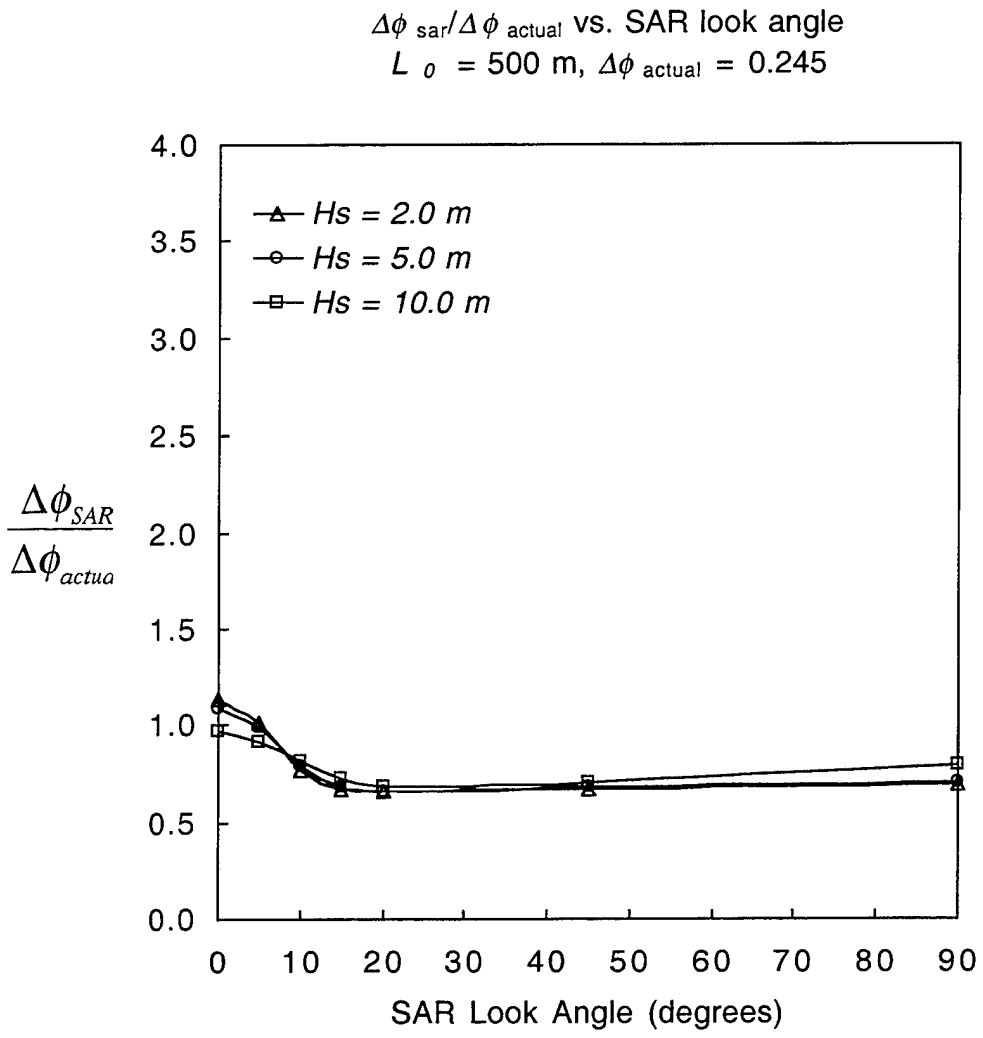

Figure 5 Apparent directional spread $\Delta\phi_{SAR}$ from simulated SAR image, normalized by actual directional spread $\Delta\phi_{Actual} = 0.245$ for various SAR look directions relative to the dominant wave direction, with H_s = 2.0 m, 5 m and 10.0 m, and λ = 500 m.

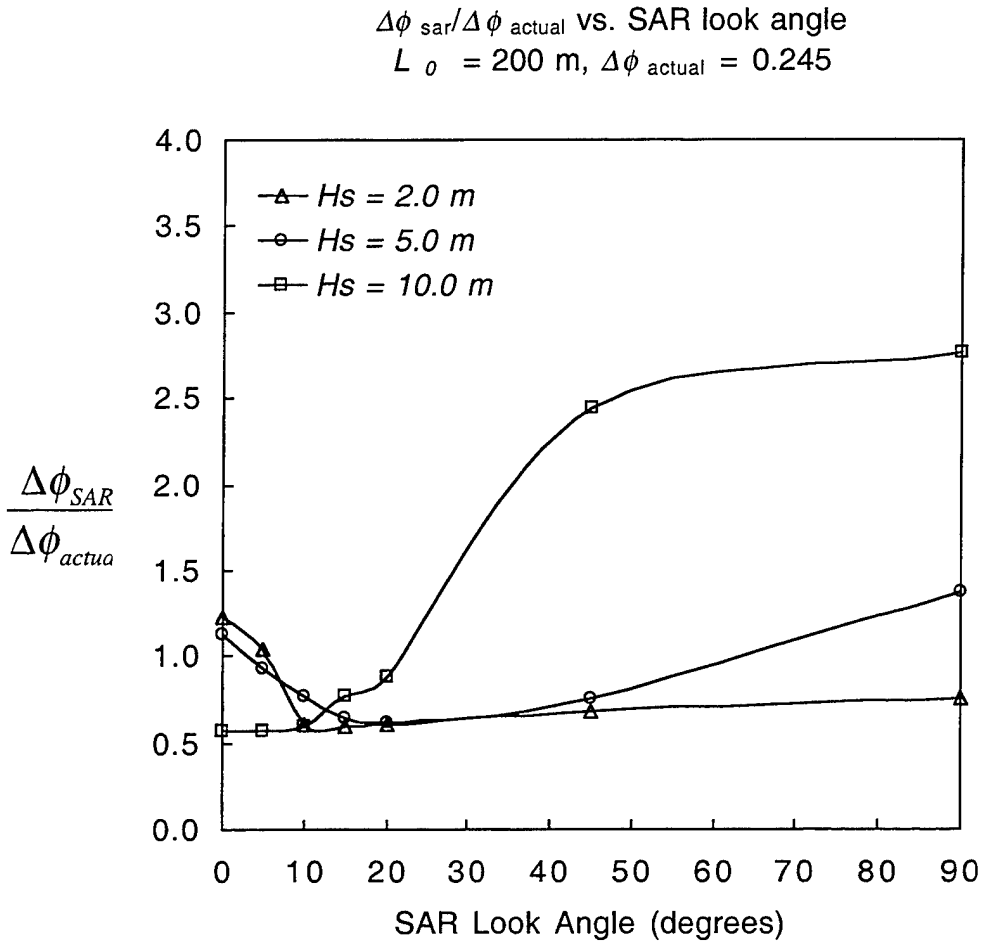

Figure 6 Apparent directional spread $\Delta\phi_{SAR}$ from simulated SAR image, normalized by actual directional spread $\Delta\phi_{Actual} = 0.245$ for various SAR look directions relative to the dominant wave direction, with H_s = 2.0 m, 5 m and 10.0 m, and λ = 200 m.

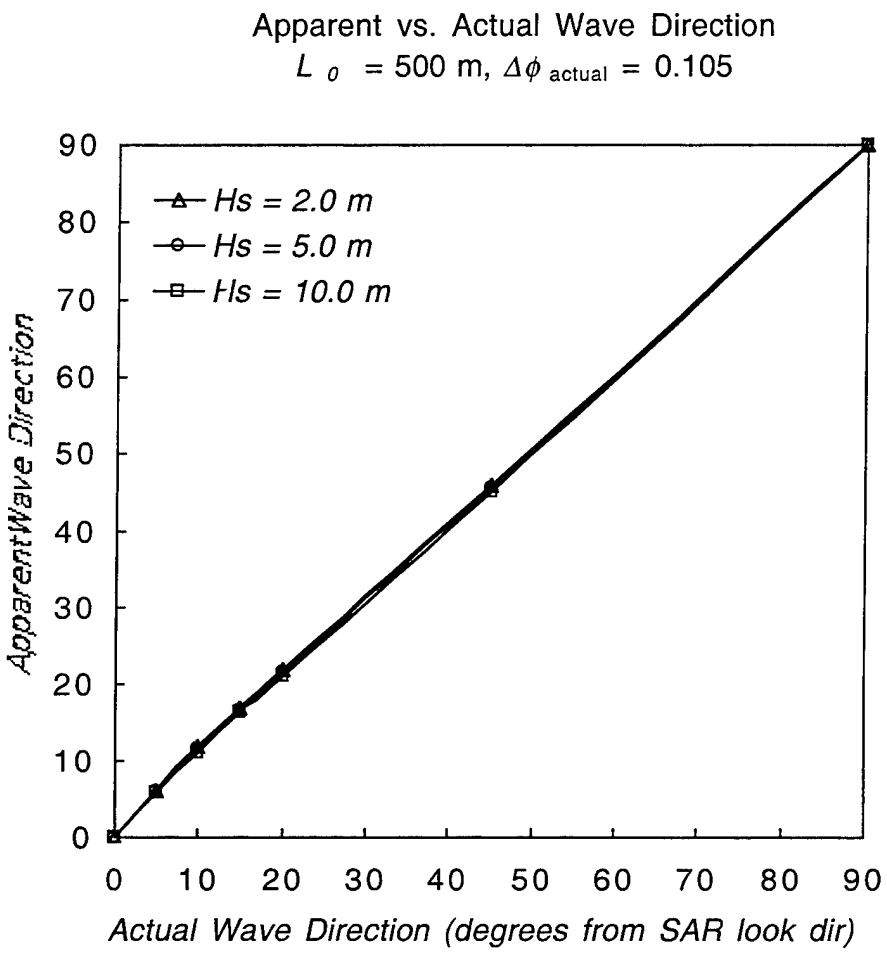

Figure 7 SAR Look Direction vs Apparent Wave direction for $\Delta\phi_{Actual} = 0.105$ vs. SAR look direction with H_s = 2.0 m, 5 m and 10.0 m, and λ = 500 m.

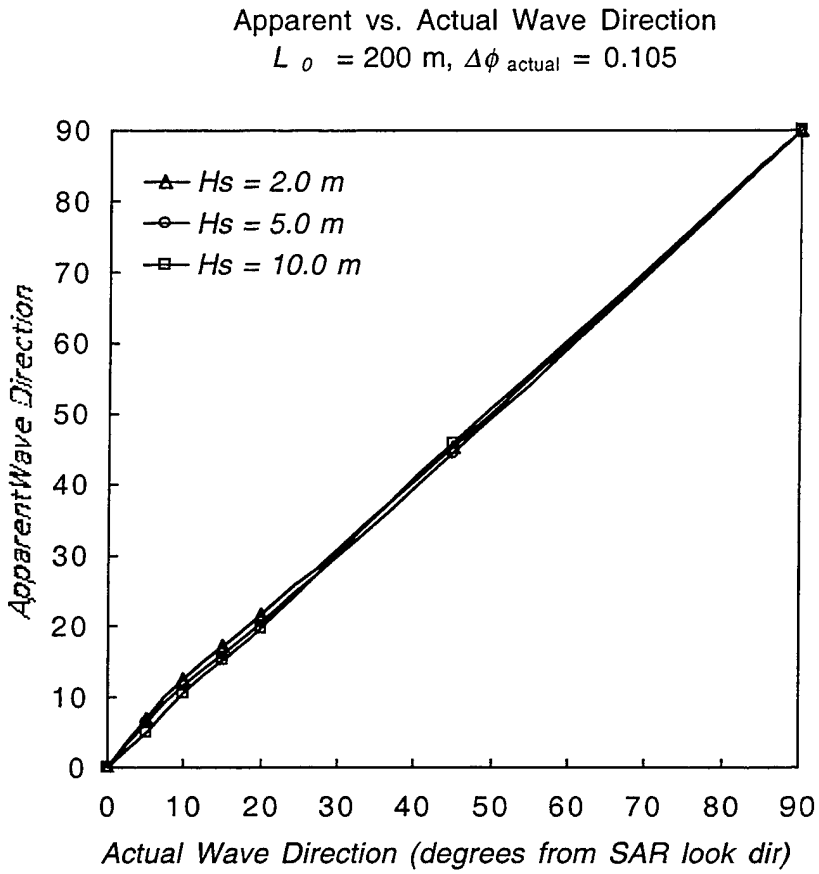

Figure 8 SAR Look Direction vs Apparent Wave direction for $\Delta\phi_{Actual} = 0.105$ vs. SAR look direction for H_s = 2.0 m, 5 m and 10.0 m and λ = 200 m.

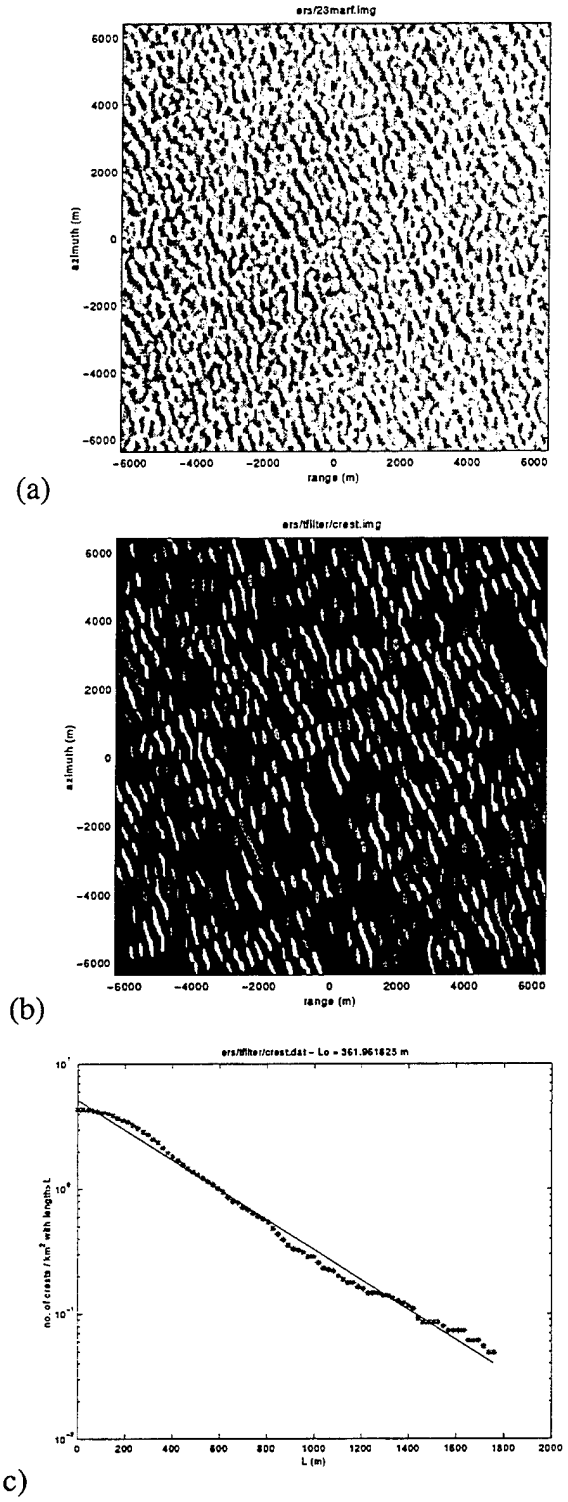

Figure 9 Results for ERS SAR image (©ESA 1997) of waves in the Labrador Sea; a) filtered SAR image, b) wave crests identified in SAR image, and c) crest length distribution.

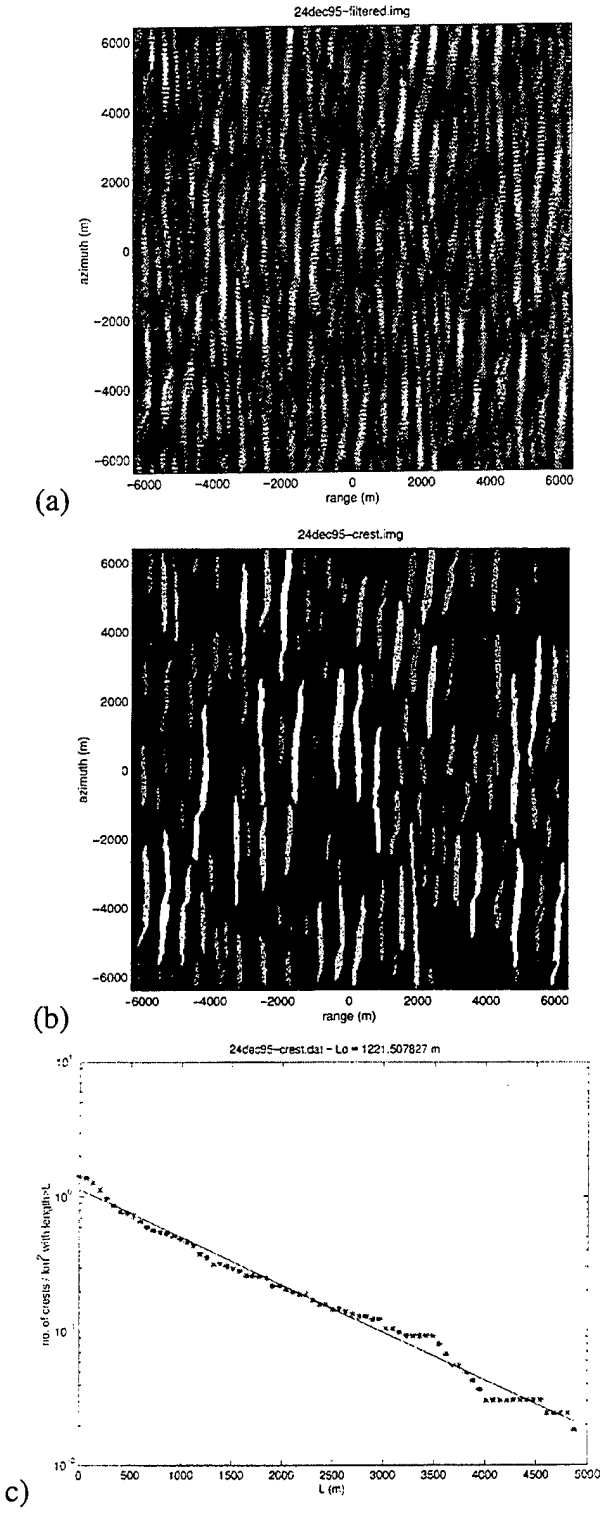

Figure 10 Results for ERS SAR image (©ESA 1995) of waves off the Oregon coast; a) filtered SAR image, b) wave crests identified in SAR image, and c) crest length distribution.

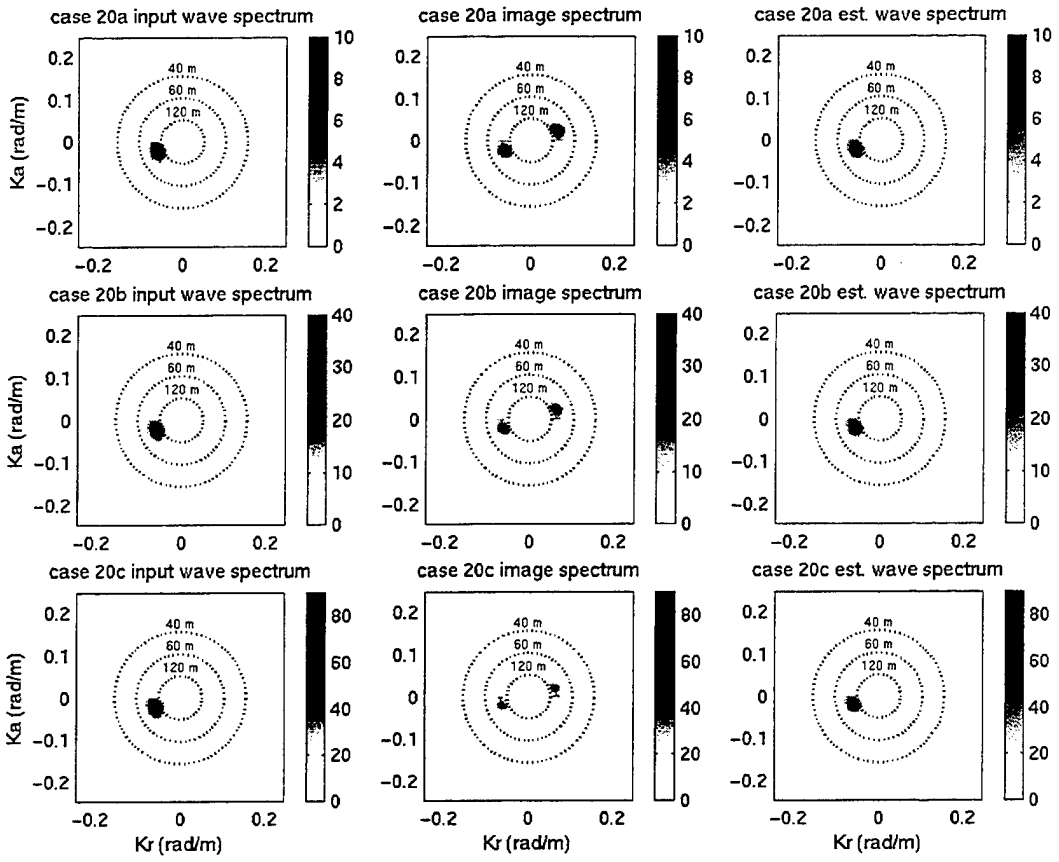

Figure 11 Forward-backward results using assumed wave spectra (left column) with $\lambda_p = 100$m, $\phi_p = 20°$, and $H_s = 0.5$m (top), 1.0m (middle), and 1.5m (bottom). Center column shows simulated image spectra and right column shows estimated wave height spectra.

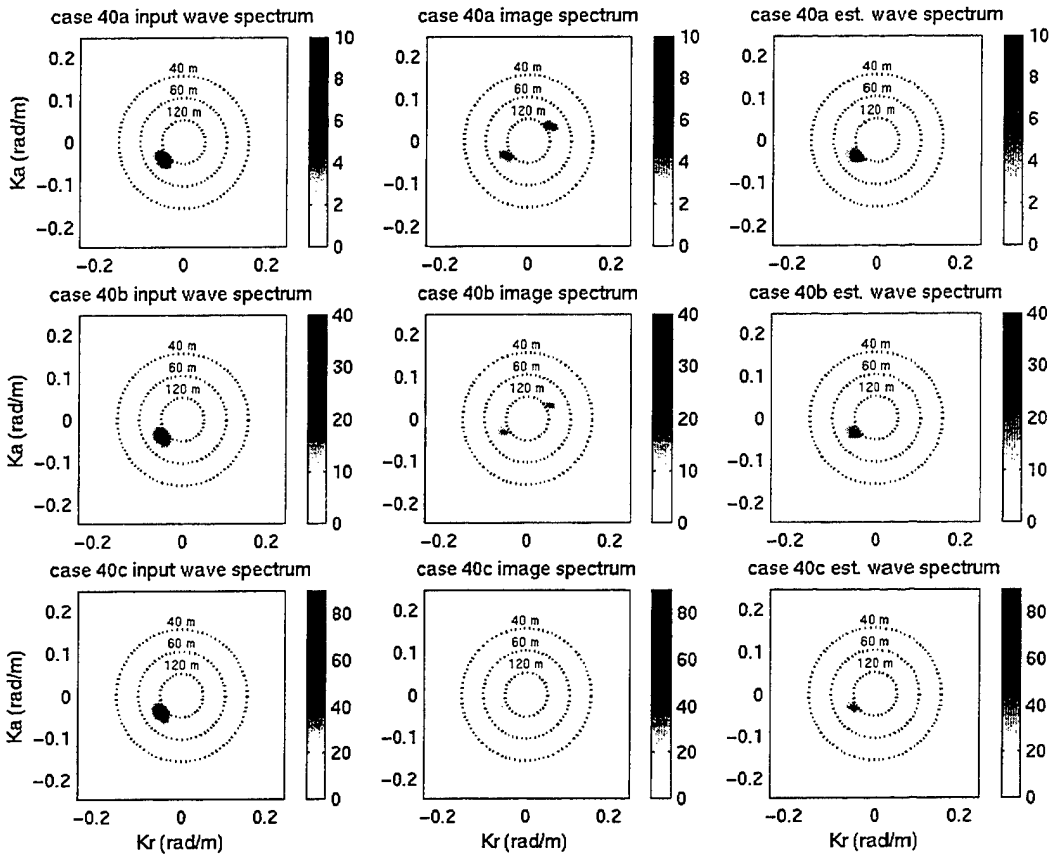

Figure 12 Forward-backward results using assumed wave spectra (left column) with $\lambda_p = 100\text{m}$, $\phi_p = 40°$, and $H_s = 0.5\text{m}$, and $H_s = 0.5\text{m}$ (top), 1.0m (middle), and 1.5m (bottom). Center column shows simulated image spectra and right column shows estimated wave height spectra.

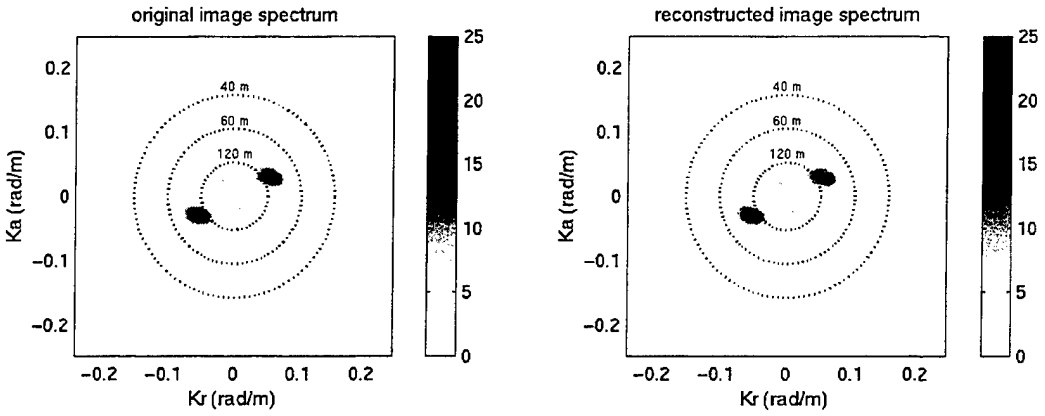

Figure 13 Image spectra calculated from the input wave spectrum (left panel) and from the estimated wave spectrum (right panel), for $\lambda_p = 100\text{m}$, $\phi_p = 40°$, and $H_s = 1.5\text{m}$.

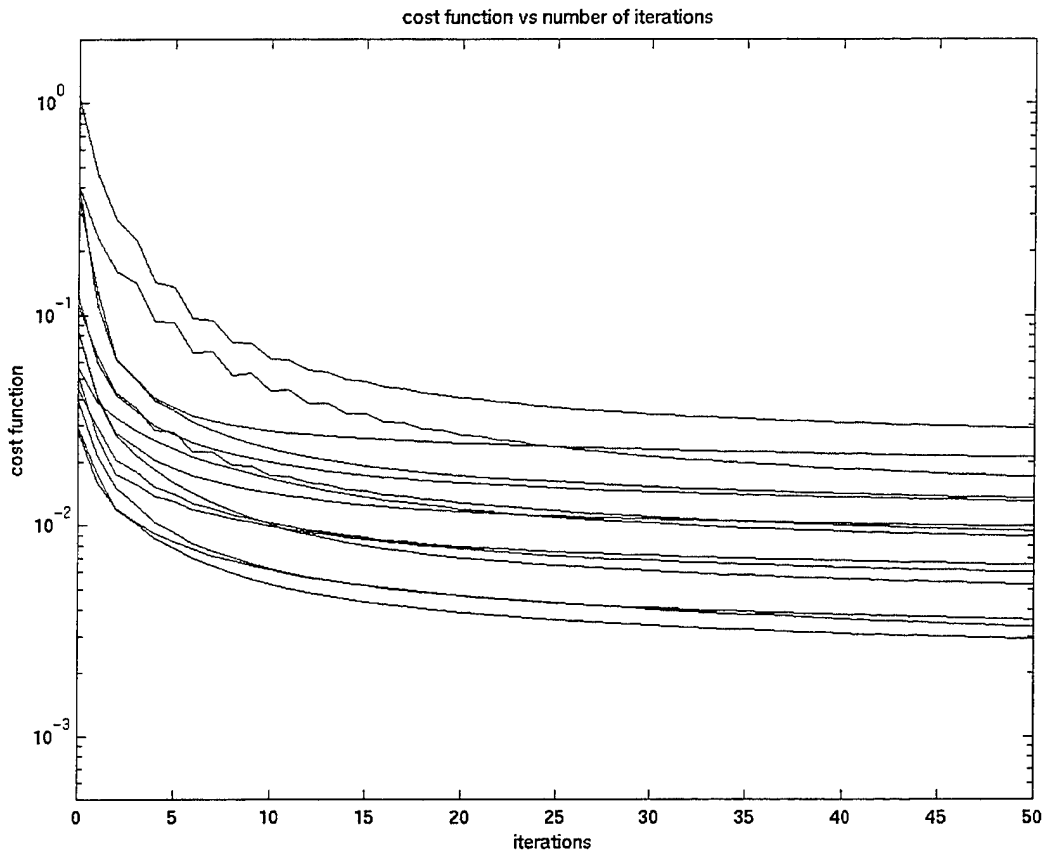

Figure 14 Cost function versus iteration number for all ERS data sets.

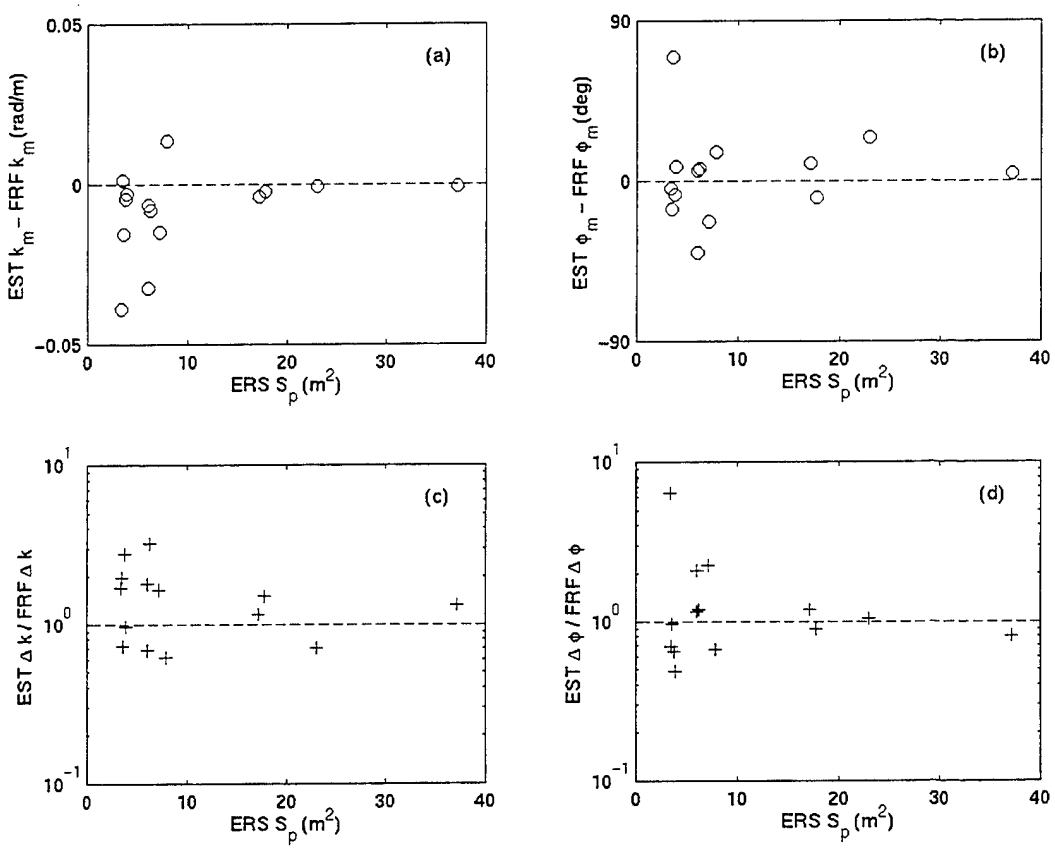

Figure 15 Differences in (a) mean wavenumber, (b) wave direction, (c) wavenumber width, and (d) angular width obtained from estimated wave spectra and from FRF spectra, plotted versus the peak spectral density in the ERS image spectrum.

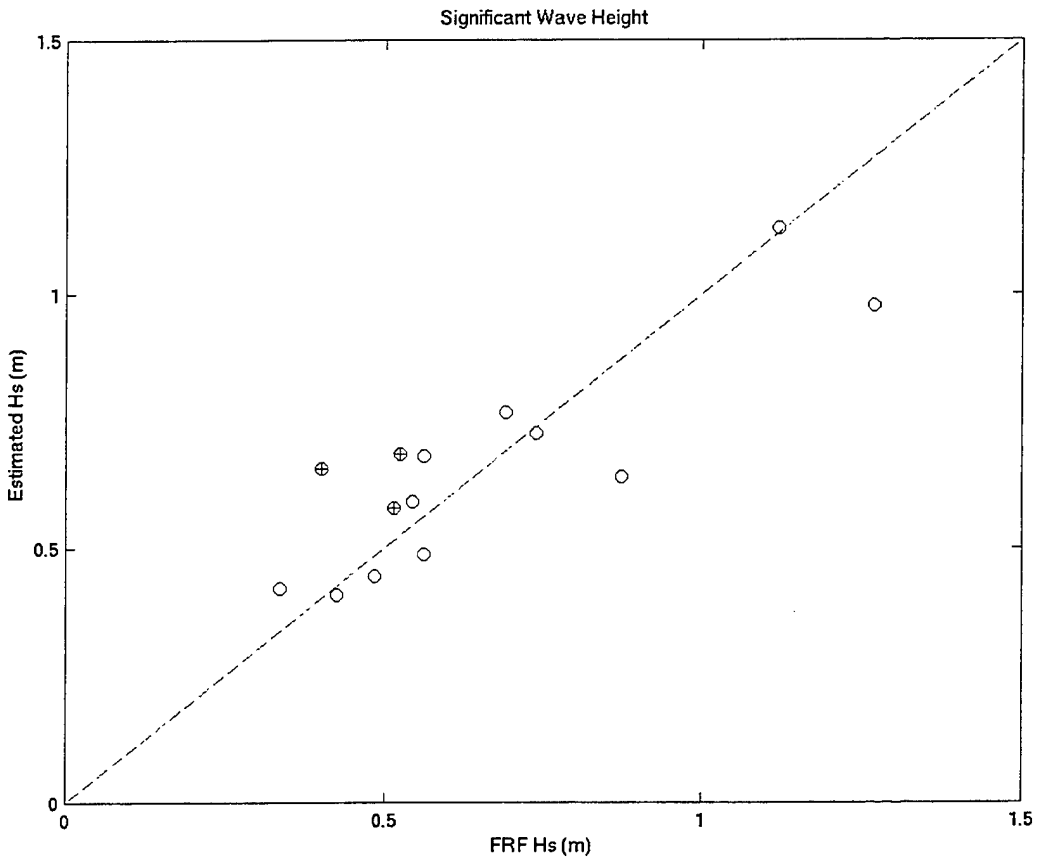

Figure 16 Significant wave heights estimated from ERS images versus those obtained from FRF measurements.

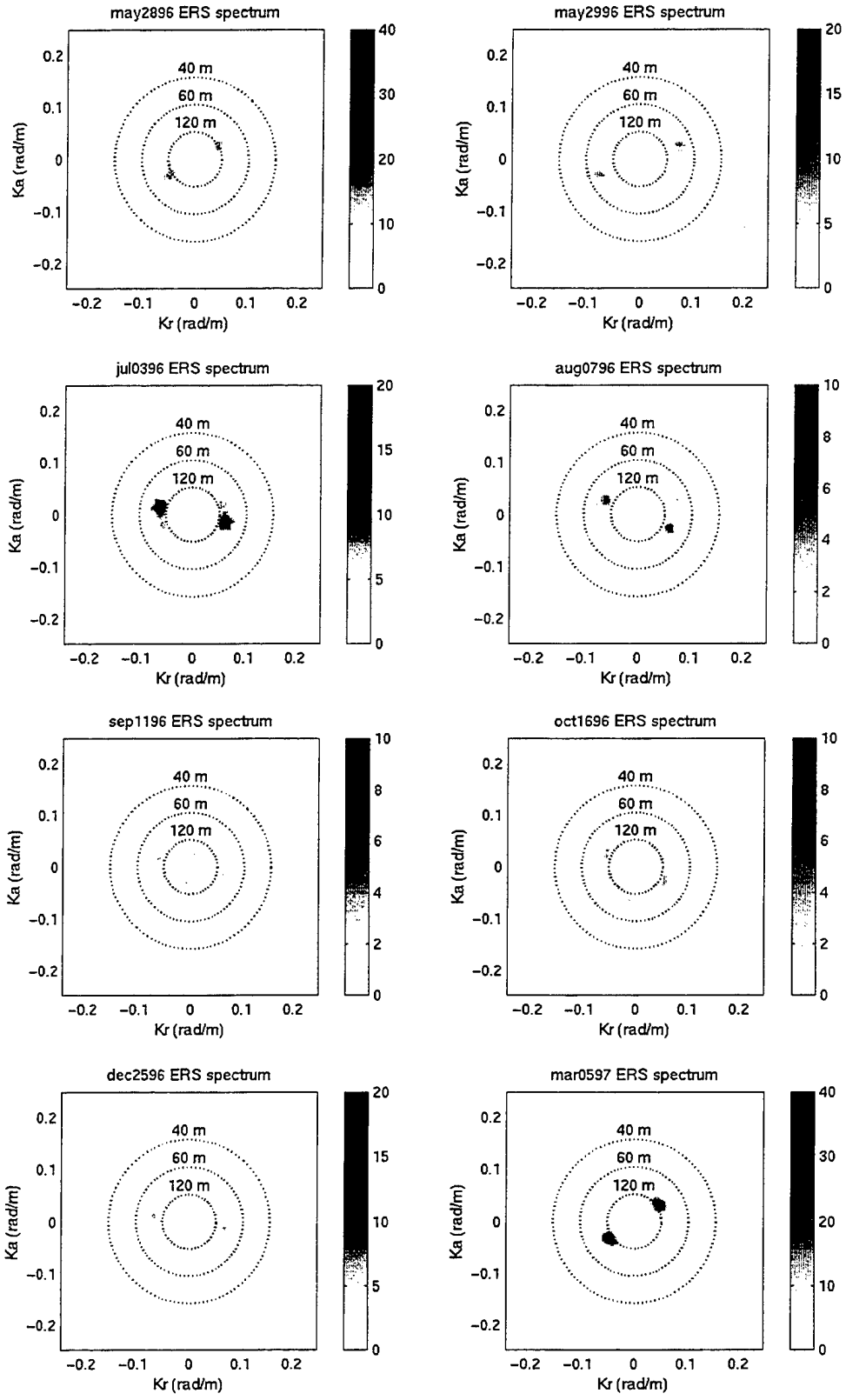

Figure 17 ERS Image Spectra

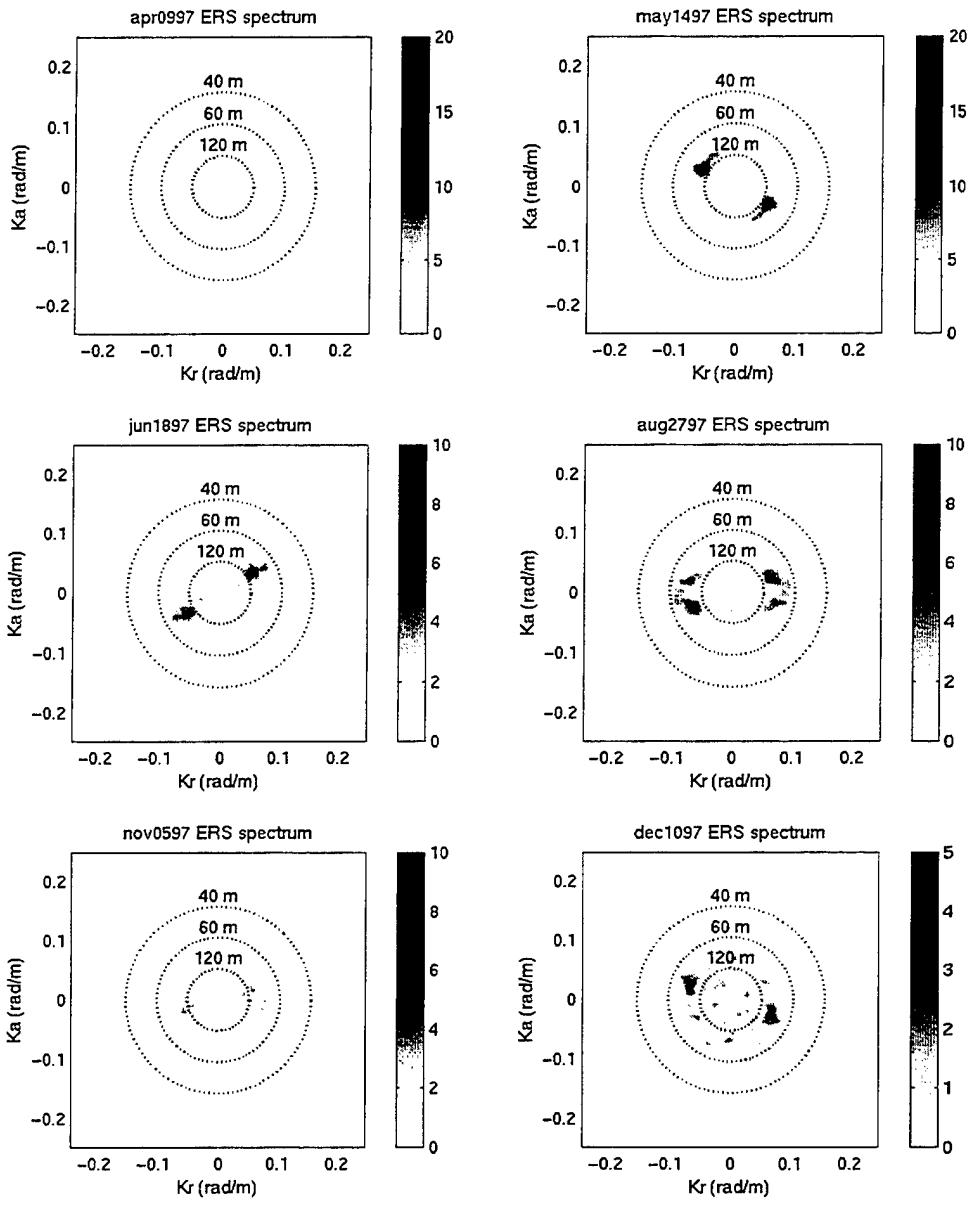

Figure 17 (Continued)

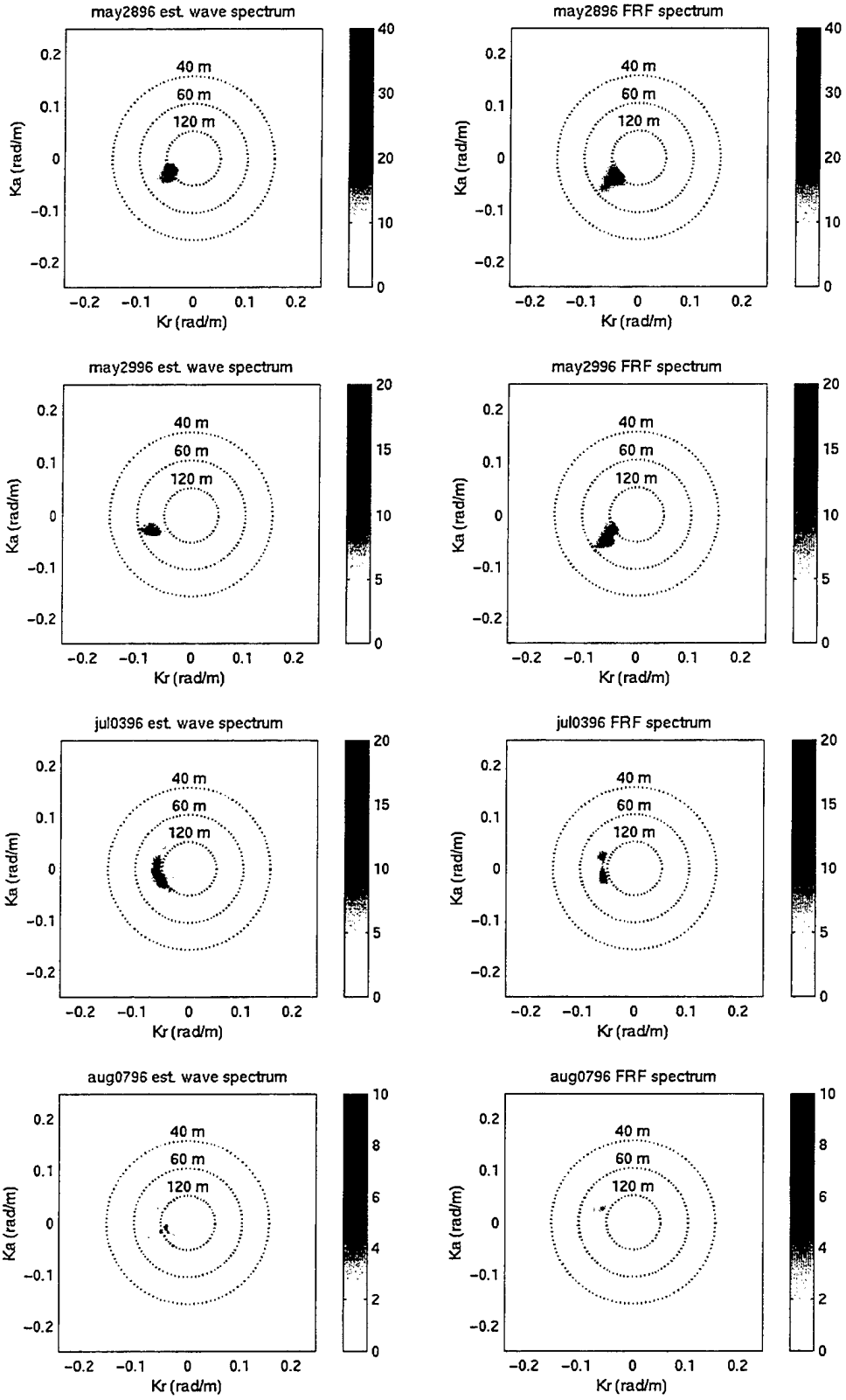

Figure 18 Estimated and Measured (FRF) Wave Height Spectra

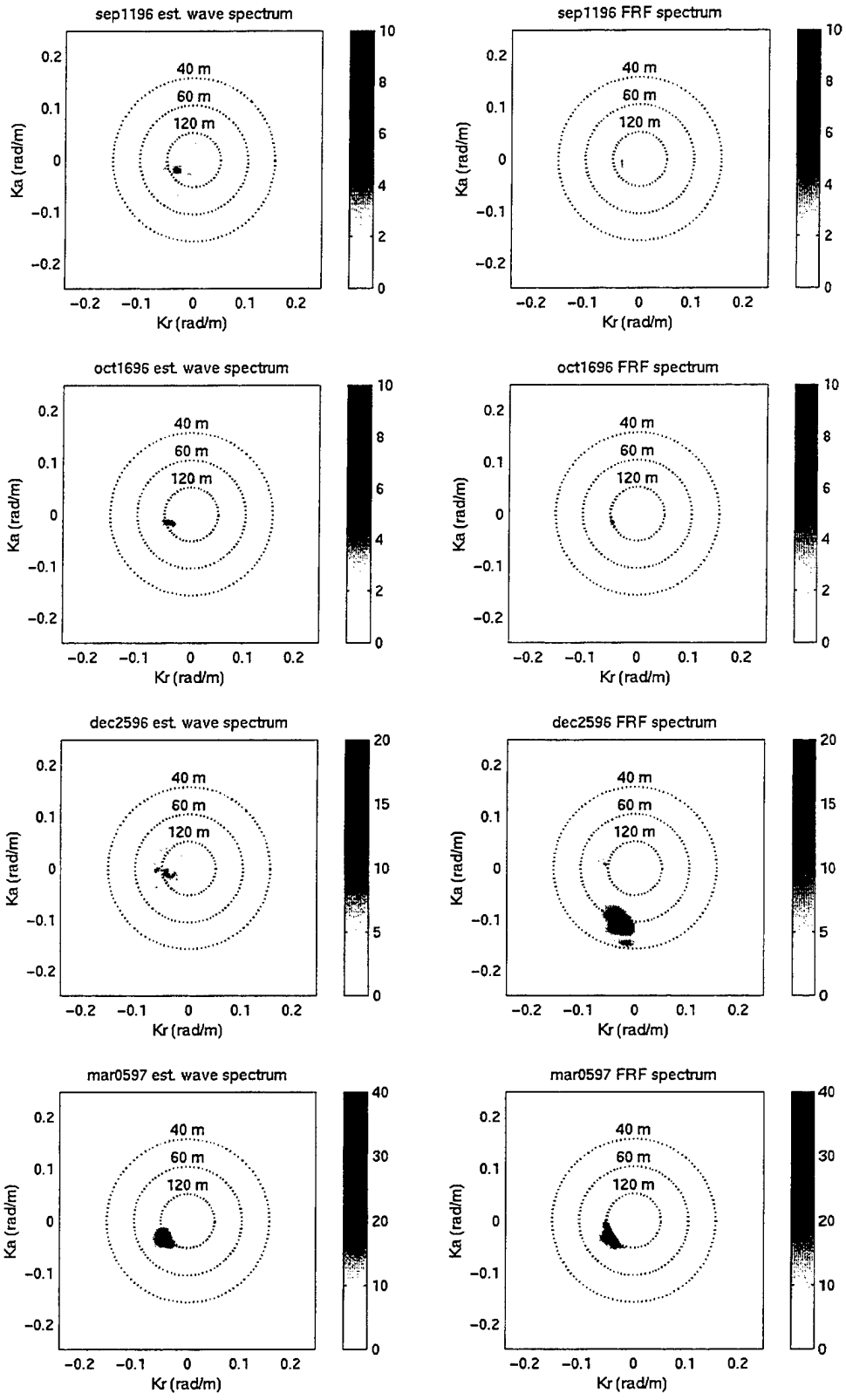

Figure 18 (continued)

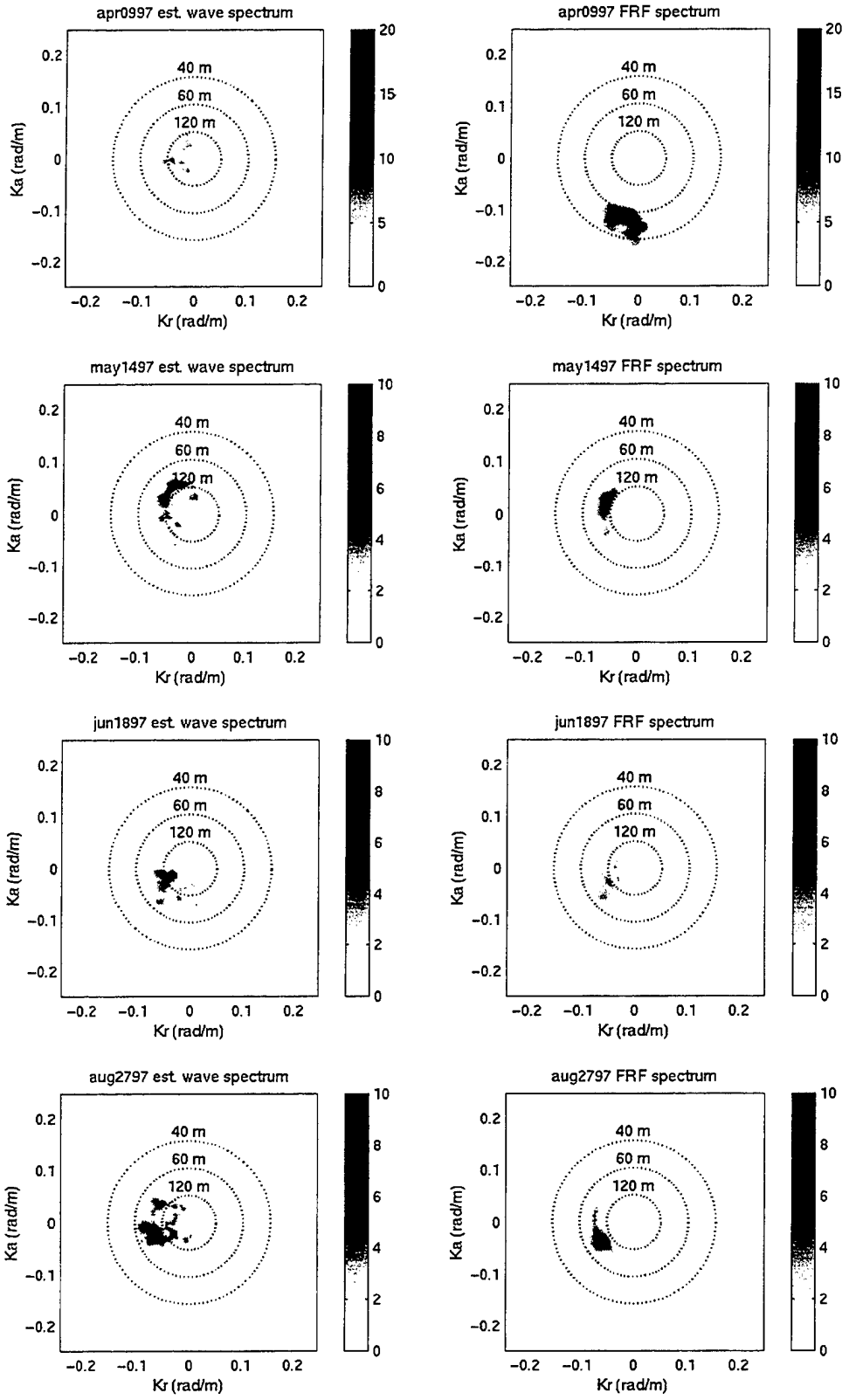

Figure 18 (continued)

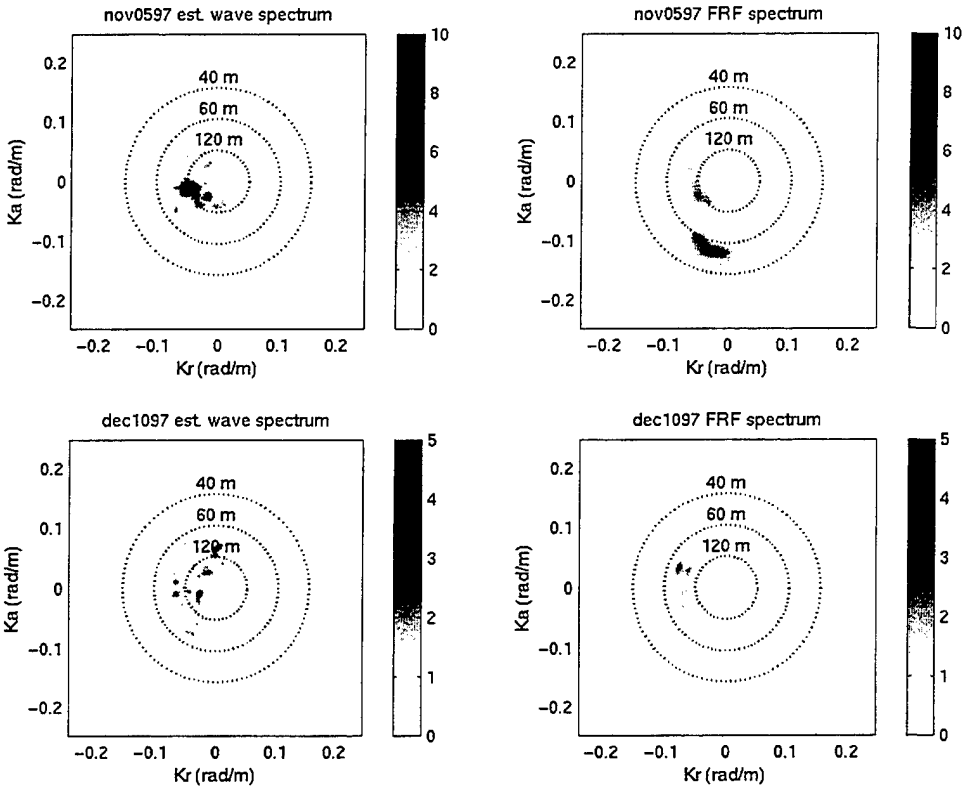

Figure 18 (continued)